A Master thesis in the Nanoscience Curriculum to obtain the dignity of a
Master of Science in Nanosciences

Towards the Inverted Cyanine-Dye Solar Cell

Development of titanium oxide thin-films for charge-carrier collection in cyanine-dye hybrid organic solar cells

Submitted to Prof. Ernst Meyer, Department of Physics, University of Basel, Switzerland
Supervisor: Dr. Roland Hany, Lab for Functional Polymers, EMPA Dübendorf, Switzerland

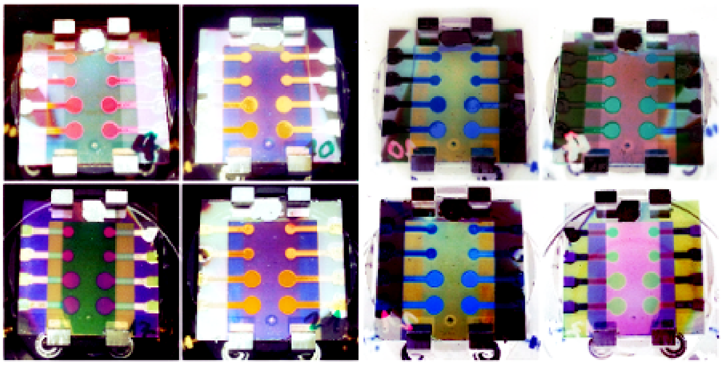

Etienne Berner

etienne.berner@stud.unibas.ch

September 2, 2012

Abstract:

Organic solar cells are considered as potential low cost renewable energy resources. Research in this field has gained a lot of interest in recent years and development of new device structures and steadily improved performances are reported on a regular basis. In this work, the inverted configuration of a cyanine-dye bilayer heterojunction solar cell was evolved.

One disadvantage of the regular geometry is its sensibility to oxygen and water. When the solar cell comes in contact with oxidizing agents in ambient air, it degrades quickly. The inverted geometry for polythiophene based solar cells is reported to be much more stable in air as the regular configuration, therefore the inverted geometry for cyanine based solar cells was of interest as well.

The inverted structure consists of an electron collecting layer at the ITO bottom electrode. For this objective, titanium oxide thin films were fabricated by reactive RF magnetron sputtering or via spin-coating of a TiO_2 nano-particle suspension. These films were characterized regarding the crystallinity, conductivity, surface roughness and absorbency spectra. The working principle was proved by polythiophene based inverted solar cells, which reached a maximum efficiency of $\eta = 3.27\%$.

In a second step, inverted cyanine-dye solar cells were fabricated. With layer thickness optimizations of the electron accepting C_{60} and hole collecting MoO_3, efficiencies approaching 3% were achieved. This is among the highest reported efficiency for cyanine based solar cells. With regard to stability, first experiments delivered promising results.

Contents

List of Abbreviations

C_{60}	Fullerene, also known as C_{60} buckyball
AFM	Atomic force microscope
BHJ	Bulk heterojunction
CB	Chlorobenzene, a solvent
Cy-3	Cyanine-dye, containing three methine groups linking two indole end-groups
GIXRD	Grazing incidence X-ray diffraction, used for thin-film analysis
HJ	Heterojunction
I/V	Electrical current[Ampere]/voltage[Volts]
ITO	Indium tin oxide, a transparent conducting metal-oxide
OPV	Organic photovoltaics
P3HT	Poly(3-hexylthiophene), a polythiophene, used as light-absorber
PCBM	Phenyl-C61-butyric acid methyl ester, a fullerene derivative
PE	Polyethylen, contained in syringes
PEDOT:PSS	Poly(3,4-ethylenedioxythiophene): poly(styrenesulfonate), a transparent, current conductive polymer
PES	Polyethersulfone, used for filter membranes
PP	Polypropylen, contained in syringes

ppm	Parts per million
PTFE	Polytetrafluoroethylene, Teflon, used for filter membranes
PV	Photovoltaics
PVC	Polyvinylchlorid
TFP	Tetrafluoropropanol, a solvent
UV-Vis	Ultraviolet-visible spectroscopy, used for thin-film analysis
XRD	X-ray diffraction

1. Introduction

1.1. Motivation

The daily energy consumption in our society is omnipresent. There is no travel today without noticing somebody playing on a "smartphone". Traffic and internet are just two keywords to name. And since energy can not be produced, but only transformed, mankind transforms energy mainly by burning resources. As long as renewable resources are burned, this is no problem.

In Switzerland, most of the consumed energy is based on products of crude oil (54%) [1]. Thereof around 19% are requested for heating, the remaining 35% are used to drive vehicles. Petroleum gas makes 12% of the consumed energy, mostly for heating purposes. 25% of the consumed energy in Switzerland is electricity. In 2011, $58'599$ GWh were inquired. Worldwide, more than 80% of demanded energy is accessed by fossil fuels including gaz, oil and coal.

Electricity is the most valuable energy form because it can run all sort of machines and utilities. It is the most universal energy, but has one disadvantage: its storage is not possible for large amounts yet. Energy storage and transportation are crucial for energy supply. Up to now, most energy is shipped with huge tankers from one continent to another or pumped in pipelines over long intercontinental distances. It is clear, that during such transports of valuable goods, conflicts and dependencies can rise and at one point the stores are empty.

To refill the energy stores, the sun is the only supply. All fossil fuels originated from carbonised plant remainings over millions of years. Consequently, the sun was the energy source since life existed on our planet. Therefore, direct transformation of sunlight into usable energy is of high interest for an enduring society.

The simplest way using the sunlight is to directly heat up a media, also known as solar heating. Solar heating can be used to cook for instance, but it is of higher interest to heat up large amounts of water and big buildings. There are promising applications available, its potential is undoubted and further extensions of installations can be expected.

Another possibility for sunlight transformation are photovoltaics (sec.2.1). Sunlight is absorbed and directly transformed into electrical current. This fascinating process could help to overcome the problem of running out resources.

In 2011, photovoltaics covered with 149 GWh (in 2009: 50 GWh) 0.25% of the electrical power in Switzerland [1]. In Germany, this fraction has tripled between 2009 and 2011 from 1.06% to 3.1% [2]. Obviously, it is still considered to be a niche product, but there is a huge potential to increase the portion of solar power. With further development of this technology, it will hopefully become cheaper, more effective and widely accepted as supplementary energy resource.

1.2. Goal of the Work

In the functional polymers lab at EMPA, usually the regular geometry of cyanine based organic solar cells were fabricated. During this six month master thesis, development of the inverted geometry should be realised. The standard geometry includes as top electrode a low work function metal, sensitive to oxygen and water. In the inverted geometry, a metal with a high work function is deposited as top contact. This could enhance the lifetime of the solar cell. The inverted geometry requires an electron collecting layer at the bottom electrode (ITO). Titanium-oxide was chosen for this purpose. Development includes characterization of differently fabricated Ti-oxide thin films and comparison in solar cell devices.

2. Theoretical Background

2.1. Photovoltaics

Known since Bequerel's photo-electrical element dating back to 1839, the photo-electrical effect was explained by Einstein in 1907 based on his light quantum theory [3]. In photovoltaics (PV), absorption of sunlight generates an electrical current. In the Bell laboratories, first crystalline Si solar cells with efficiencies of 4-6% were fabricated by Fuller et al. in 1954 [4]. The technology developed and today's record solar cells based on crystalline Si have efficiencies of 25.0% [5].

The record cells for crystalline bulk semiconductors reached almost the highest theoretically possible power conversion efficiencies. The physics of crystalline solar cells is established and many books explain basic principles of PV and the theoretical limits (e.g.[6][7][8]). To summarize, excitons can be generated by photon absorption in the bulk. These excitons diffuse to a region, where they can split up due to an internal electrical field (e.g. pn-junction) into charge carriers (electrons and holes). The charge transport to anode, resp. cathode results in an electrical current.

The market for PV modules today is dominated by poly- and mono-crystalline Si solar cells with typical efficiencies of $\eta \sim 13 - 17\%$. The high production costs originate mostly during pure Si wafer fabrication.

2.1.1. Characterization of Solar Cells

To compare different solar cells, common test conditions are prerequisite and defined by industrial standards. The standard illumination to measure a solar cell is under air mass (AM) 1.5 radiation with intensity of 1000 W/m^2, which simulates sunlight reaching the earth's surface under a solar zenith angle of $\alpha = 48.2°$. The PV module has a temperature of 25°C during measurements.

Characteristics of solar cells are obtained by analysis of the current-voltage (IV) curves. Fig.2.1a shows an example for IV curves of an organic solar cell. Dashed line is measured in the dark (diode behaviour), the full line is measured under illumination. At point (a) in Fig.2.1a, zero voltage is applied between anode and cathode. Under these short-circuit conditions, in the dark there is no current. Under illumination, separated charge carriers can drift due to the internal electrical field to respective electrodes. This is called the short-circuit current I_{sc}. In (b), there is zero current flow between the electrodes. The applied voltage balances the internal electrical field and does not allow any charge carriers to flow. This voltage is called open-circuit voltage V_{oc}.

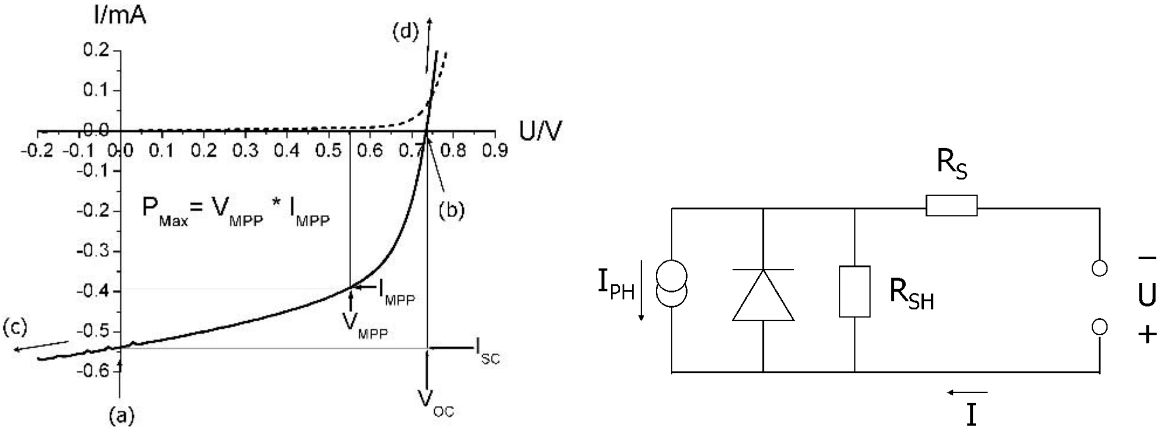

(a) Current-voltage curves of an organic solar cell, from [9]. Dashed line is in the dark, the full line under illumination.

(b) Equivalent circuit for a solar cell, from [9].

Figure 2.1.: Solar cell analysis.

The power of a solar cell is the product $P = I \cdot V$ at any point on the IV curve. The point with the highest power is called maximum power point (MPP) and hence $P_{max} = I_{mpp} \cdot V_{mpp}$. The fill-factor (FF) is the fraction of accessible power at the MPP compared to the product of V_{oc} and I_{sc}. It is given by

$$FF = \frac{I_{mpp} \cdot V_{mpp}}{I_{sc} \cdot V_{oc}} \tag{2.1}$$

The efficiency η of a solar cell depends on the solar cell's output power P_{cell} at the MPP and the incoming radiation power P_λ. It is given by

$$\eta = \frac{P_{cell}}{P_\lambda} = \frac{I_{mpp} \cdot V_{mpp}}{P_\lambda} = \frac{FF \cdot I_{sc} \cdot V_{oc}}{P_\lambda} \tag{2.2}$$

Consequently, increasing of efficiency means increasing FF, I_{sc} and/or V_{oc}.

In Fig.2.1b an equivalent circuit for a solar cell is shown. Real solar cells have electrical losses, which are modelled using series and parallel resistances. R_S is the series resistance, which is the sum of all series resistance contributions for charge carriers to reach their electrode such as crossing contacts and interface transfer. For a high FF, R_S should be very low. R_{SH} is the shunt, or parallel resistance, which should be high in order to prevent leakage currents. The IV characteristics for this one-diode model is described by

$$I(U) = I_0(e^{\frac{e}{nk_BT}(U-IR_S)} - 1) + \frac{U - IR_S}{R_{SH}} - I_{PH} \tag{2.3}$$

with I_{PH} as the photo-current, e the elementary charge, n the diode quality factor and U the applied voltage.

In Fig.2.2 ideal resistances $R_S = 0\Omega$ and $R_{SH} = \infty$ are indicated with curve 1. Curve 2 has $R_S = 0\Omega$ but $R_{SH} = 50\Omega$, which cause leakage currents and lower FF. Curve 3 considers the case with a serial $R_S = 5\Omega$ and $R_{SH} = \infty$.

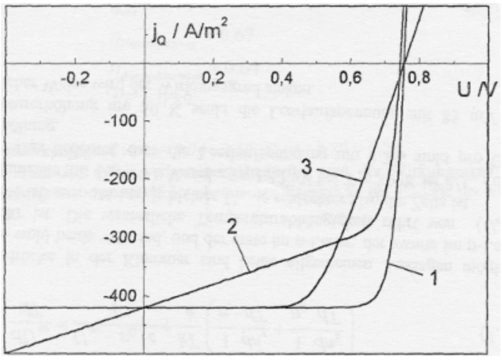

Figure 2.2.: Ideal resistances $R_S = 0\Omega$ and $R_{SH} = \infty$ for curve 1 result in a high FF. Curve 2 considers lower R_{SH}, curve 3 higher R_S. Figure is from [6].

2.1.2. Organic Photovoltaics

Organic photovoltaics (OPV) were developed over the last three decades and today different approaches are available and steadily improved. OPV is considered as alternative to conventional *Si* solar cells due to potential low cost material and small energy consumption during fabrication. OPV can be deposited on flexible substrates, in different colours and can offer more creative applications than conventional *Si* based PV.

A first milestone in OPV was achieved by Tang [10] in 1985, who implemented a planar organic bilayer heterojunction (Fig2.3a) sandwiched in between gold as top and indium tin oxide (ITO) as transparent bottom electrode. The bilayer consisted of copper phtalocyanine as electron donor (p-type semiconductor) and a perylene derivative as e$^-$ acceptor (n-type). His solar cell reached an efficiency of $\eta \sim 1\%$.

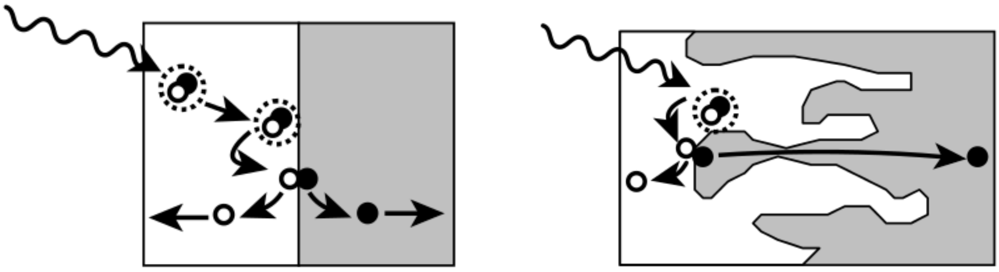

(a) Planar bilayer heterojunction

(b) Bulk heterojunction (BHJ)

Figure 2.3.: Schematic charge carrier generation in solid state organic solar cells: The incoming photon is absorbed and an exciton is generated. It diffuses to the heterojunction, where it separates into charge carriers. Figures from [11]

In 1991, Grätzel introduced the concept of the dye-sensitized solar cell (DSSC) [12]. These solar cells are based on two electrodes, which are connected by a liquid electrolyte used as redox-chemical. Today, the highest reported DSSC efficiency is $\eta = 10.5\%$ [5].

Development of conducting and semiconducting polymers lead to incorporation of these into solar cell devices. In 1995, the concept of a bulk heterojunction (BHJ, see Fig.2.3b) between a semiconducting polymer and an electron accepting fullerene derivative was presented [13]. This is today the most important conception for solid state, solution processed organic solar cells. Most prominent materials for BHJ are Poly(3-hexylthiophene) (P3HT, Fig.2.4a) as light absorbing semiconductor (p-type) and Phenyl-C61-butyric acid methyl ester (PCBM, Fig.2.4b) as solution processable fullerene derivative, which is the electron accepting material. The BHJ concept is advantageous over the planar HJ because of a larger heterojunction interface and hence a higher probability for charge carrier generation.

With the development of regioregular P3HT [14], its analysis (e.g.[15]) and further improvements, the P3HT/PCBM solar cell reached higher efficiencies after annealing [16] and was further developed [17] to reach $\eta \simeq 5\%$. With development of new polymers, the record for a organic polymer solar cell is $\eta = 8.3\%$ [5].

In Fig.2.4, the chemical structures of used chemicals (see sec.3.3) are shown. PEDOT:PSS is a conductive, transparent polymer used as p-type electrodes in many polymer based solar cells. The cyanine dye (Cy-3, Fig.2.4c) used for cyanine based solar cells (sec.3.5.3) is deposited on fullerene (C_{60}), forming a planar bilayer heterojunction. Zonyl (Fig.2.4f) is a fluorosurfactant to enhance wetting (sec.3.4.3 and 4.1.6).

As there are hundreds of material combinations and fabrication methods reported, editors recently published reference books [18] [19] [20].

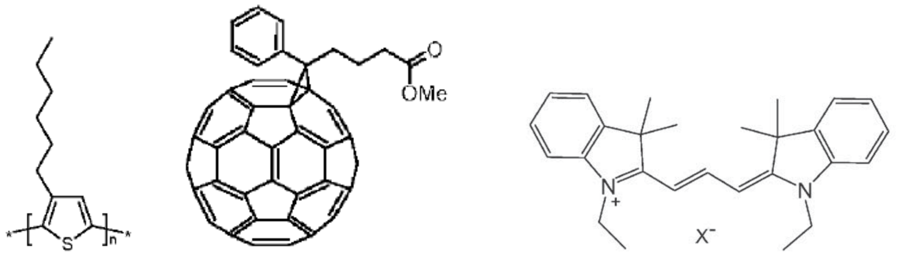

(a) P3HT (b) PCBM (c) Cyanine-dye (Cy-3). The counterion X^- was PF_6^-

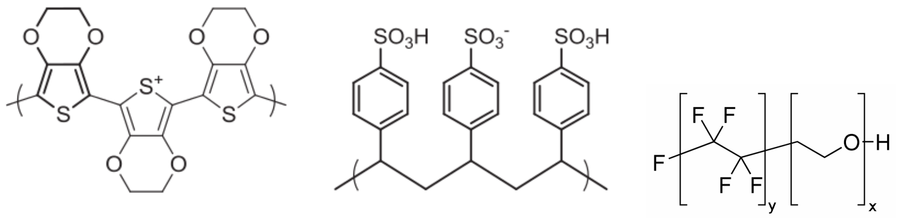

(d) PEDOT (e) PSS (f) Zonyl

Figure 2.4.: Chemical structures

2.2. Titanium Dioxide

TiO_2 exists in three crystalline polymorphs: rutile, anatase (both tetragonal) and brookite (orthorhombic). In 1942, rutile and anatase were reported to be n-type semiconductors [21]. It is one of the most investigated metal oxides and many reviews have been published. Surface science of TiO_2 is reviewed e.g. in [22], its role in DSSC in [19] and its applications in photocatalysis in [23].

Thin film fabrication methods include sputtering, sol-gel routes, sintering and spin-coating. Each method has strong influence on the final film, as well as surface preparation methods (e.g. annealing, re-oxidizing of a reduced surface) can result in dramatic changes of the initial properties. Generally, the TiO_2 surface is hydrophilic.

TiO_2 is used for many purposes, e.g. in DSSC, as (photo)catalyst, as pigments in white paint, for gas sensor applications or optical coatings. Every application has special requests on the TiO_2 property.

For inverted polymer solar cells, TiO_x films are mostly fabricated via sol-gel routes [24] [25] [26]. Analysis of sol-gel derived TiO_x is reported in [27] [28] [29].

TiO_2 films prepared by reactive radio-frequency (RF) magnetron sputtering are discussed e.g. in [30] [31] [32] [33] [34] [35] [36] [37].

3. Methods and Material

3.1. General Lab Equipment

Balances

· Mettler Toledo (Switzerland), model: SAG 105

· Mettler Toledo (Switzerland), model: XS204 DeltaRange

Glove-Box

Mecalab from Mecaplex Labortechnologie (Switzerland), manufactured in 2005. Glove-Box contents: N_2-atmosphere at room temperature, $O_2 < 5\ ppm$, $H_2O < 1\ ppm$

Plasma Cleaner

UV-Ozone Plasma cleaner from Novascan (USA), model: PSD-UV

Sputtering System

AJA International Inc. (USA), model: ATC Orion, ran by PHASE *II* J computer control from AJA International

Spin Coater

· ATM-group (Germany), model: Primus STT15

· ATM-group (Germany), model: Primus SB15

Thermal Vapor Deposition Chamber

Leybold vacuum (Germany), experimental vacuum coating system model: Univex 350 G

Vacuum Pumps

· Turbo-molecular pump from Leybold (Germany), model: Turbovac TW701 (for Univex 350 G)

· Vacuubrand (Germany), membrane vacuum pump model: MD1C (for spin coater STT15)

3.2. Analysis Equipment

Atomic Force Microscope (AFM)

NanoSurf (Switzerland), model: Mobile S used with large scan head S/N 19-04-014

Optical Microscope

Olympus (Japan), model: SZX16 (16x)

Profilometer

Ambios (USA), model: XP1, run with XP2 software

Solar Simulator

Spectra-Nova Technologies (Canada), model: S-N CTA-XS101-100x100 (Spectra-Nova Class A cell tester with integrated spectral response)

UV-Vis Spectrometer

Varian (USA), model: Cary 50 Scan

X-Ray Diffractometers

·Panalytical (The Netherlands), model: X'Pert PRO. X-Ray specs: 45 kV, 40 mA
·Bruker AXS (former Siemens)(USA), model: Kristalloflex D5000. X-Ray specs: 40 kV, 37 mA

4-wire Measurements

· Jandel (USA), four point probe head
· Keithley (USA), Model 2400 SourceMeter

3.3. Used Chemicals and Materials

Acetone

CH_3COCH_3, CAS-Nr: 67-64-1, purchased from Merck (Germany), 99.0%

AFM Tips

Pyramidal Point Probe, Non-Contact, Long cantilever with Reflex coating (PPP-NCLR), purchased from NanoSensors (Switzerland), $n^+ - Si$ ($0.01 - 0.02\ \Omega\ cm$), $f_{res} : 146 - 236\ kHz$, $k = 21 - 98\ N/m$, model: PPP-NCLR-20

Aluminium

Al-pellets, CAS-Nr: 7429-90-5 , purchased from Kurt J. Lesker Company (USA), 99.999%

Argon

Ar, CAS-Nr: 7440-37-1, purchased from Messer (Switzerland), $6.0 \equiv 99.9999\%$

Chlorobenzene (CB)

C_6H_5Cl, CAS-Nr: 108-90-7 , purchased from Sigma-Aldrich (UK), 99.8% (anhydrous)

Cyanine-dye (Cy-3)

1-Ethyl-2-[3-(1-ethyl-3,3-dimethyl-1,3-dihydro-indol-2-ylidene)-propenyl]-3,3-dimethyl-3H-indolium hexafluorophosphate, Cy-3 PF_6 cyanine dye, $C_{27}H_{33}F_6N_2P$, CAS-Nr: none, purchased from FEW Chemicals (Germany), product code: S 2108, 99.0%

Ethanol

C_2H_5OH, CAS-Nr: 64-17-5, purchased from VWR (France), 99.8%

Fullerene C_{60}

C_{60}, CAS-Nr: 99685-96-8 , purchased from SES Research (USA), 99.5%

Gloves

Sempermed (Austria), model: sempercare latex-free, powder-free nitril gloves

Hellmanex

Hellmanex III, powerful alkaline concentrate for cleaning, purchased from Hellma (Germany)

High-purity Water

H_2O, CAS-Nr: 7732-18-5, Milli-Q purifier purchased from Millipore (USA, part of the Merck-group), 0.22 μm filter, 18.2 $M\Omega\ cm \equiv$ 18.2 $\mu S/cm$

Indium Tin Oxide (ITO) on Glass

Smooth ITO for OLED and solar applications, purchased from Thin Film Devices Inc. (USA), sheet-resistance: $20\Omega/\square$, thickness: 1500 $\mathring{A}$

Isopropanol

$CH_3CH(OH)CH_3$, CAS-Nr: 67-63-0 , purchased from Merck (Germany), 99.7%

Molybdenum(VI)-Oxide

MoO_3-powder, CAS-Nr: 1313-27-5 , purchased from Sigma-Aldrich (USA), 99.99% (metal-basis)

Nitrogen

N_2, CAS-Nr: 7727-37-9 , purchased from Messer (Switzerland), $5.0 \equiv 99.999\%$

Oxygen

O_2, CAS-Nr: 7782-44-7, purchased from Messer (Switzerland), $5.5 \equiv 99.9995\%$

PCBM, a Fullerene Derivative

Phenyl-C61-butyric acid methyl ester, $C_{72}H_{14}O_2$, CAS-Nr: 160848-21-5 , purchased from Solenne BV (The Netherlands), 99%

PEDOT:PSS

Poly(3,4-ethylenedioxythiophene): poly(styrenesulfonate), $(C_6H_4O_2S)_n : (C_8H_8SO_3)_n$
CAS-Nr: 155090-83-8
· purchased from Sigma-Aldrich (China), 1.3 $wt.\%$ dispersion in pure H_2O,
PEDOT content: 0.5 $wt.\%$, PSS content: 0.8 $wt.\%$
· purchased from Heraeus (Germany), "Clevios^{TM} HTL solar", $1.0 - 1.2$ % dispersion in aqueous-based solution (unspecified)
· purchased from AGFA (Belgium), "Orgacon^{TM} EL-P5010", 3 $wt.\%$ in a thermoplastic polymer binder (unspecified)

P3HT

Poly(3-hexylthiophene), $(C_{10}H_{16}S)_n$, CAS-Nr: 104934-50-1 , regioregular P3HT purchased from Merck (Germany), "Lisicon © SP001"

Silver

Ag-pellets, CAS-Nr: 7440-22-4 , purchased from Cerac (USA, part of the Materion-group), 99.99%

Syringes

Braun (Germany), models: Inkjet 1 ml, 2 ml, 5 ml sterile, single-use polypropylen(PP)/polyethylen(PE) syringes (latex-free and polyvinylchlorid (PVC)-free)

Syringe Filters

· Pall (USA), model: Acrodisc 32mm Syringe Filter, 5 μm Supor © (polyethersulfone

(PES)) membrane

· Sun-SRi (USA), model: Titan2 yellow 17mm Syringe Filter, 0.45 μm polytetrafluoroethylene (PTFE, Teflon) membrane

·VWR (USA), model: 13mm Syringe Filter, 0.45 μm PTFE membrane

TFP

Tetrafluoropropanol, $CHF_2CF_2CH_2OH$, CAS-Nr: 76-37-9, purchased from Sigma-Aldrich (China), 98%

Thermal Vapor Deposition Boats

· Molybdenum source boat, purchased from Kurt J. Lesker (USA)

· Folded tantalum source boat with tantalum boat cover, purchased from Kurt J. Lesker (USA)

· Tungsten source boat, purchased from Leica (Germany)

Titanium

Ti-disk, CAS-Nr: 7440-32-6 , purchased from AJA International Inc. (USA), 99.999%

Titanium-Oxide Nanoparticle Suspension

TiO_2-anatase, CAS-Nr: 1317-70-0, purchased from Solaronix (Switzerland), "Ti-Nanoxide HT-L/SC", suspension (alcohol, water, acids) containing 3 $wt.\%$ TiO_2 nanoparticles with $\oslash \sim 9\ nm$

Zonyl ©

$F(CF_2CF_2)_y(CH_2CH_2O)_xH$, where $1 \leq x \lesssim 25$ and $1 \leq y \lesssim 9$, CAS:197664-69-0, Zonyl FS-300 fluorosurfactant, purchased from Sigma-Aldrich (USA), $\sim 40\ wt.\%$ solids in H_2O, 1.10 $g/ml(20°C)$

3.4. Processings

This section summarizes the experimental procedures during solar cell fabrication. For lab impressions, see Fig.3.1. Fig.3.1a shows the digitally controlled glove-box with N_2-atmosphere, in which most layers were deposited. The glove-box assembly consisted of two main boxes, which were connected together by a cylindrical channel equipped with a transportation platform. Box1 was used for spin-coating, chemical/sample storage and substrate annealing. The thermal evaporation chamber is integrated in box2, where the samples were mounted on the air-tight sample holders for performance measurements. By purging the locks (there is one for each box) with N_2, samples, lab supplies, etc. could be entered resp. sorted the glove-box. Fig.3.1b shows the sputtering setup in the lab for thin films and photovoltaics, EMPA Dübendorf, which was used to sputter Ti-oxide thin-films, see the following sec.3.4.2.

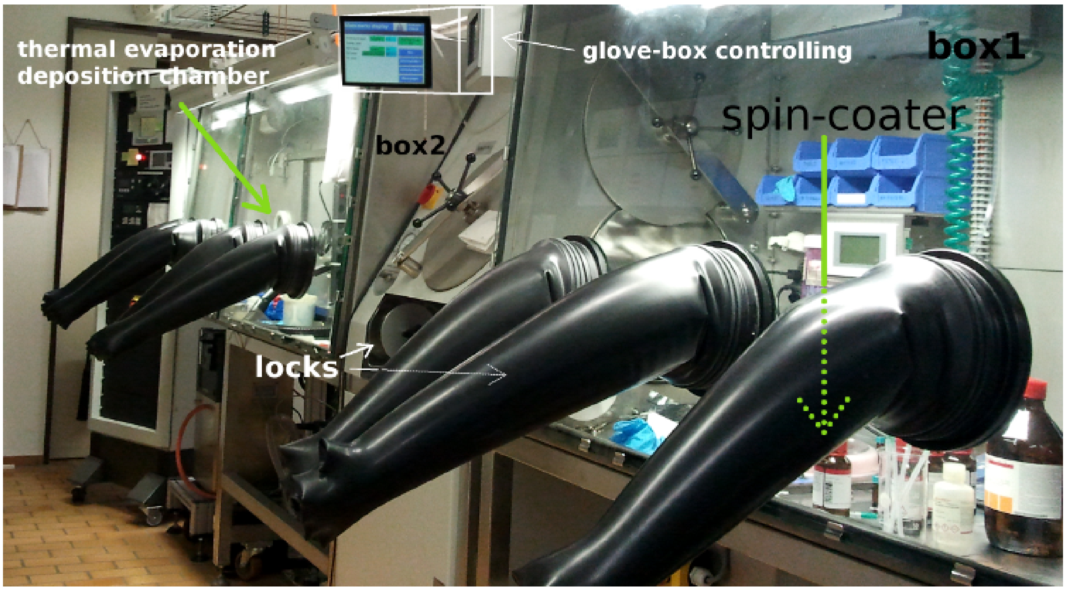

(a) Glove-box assembly

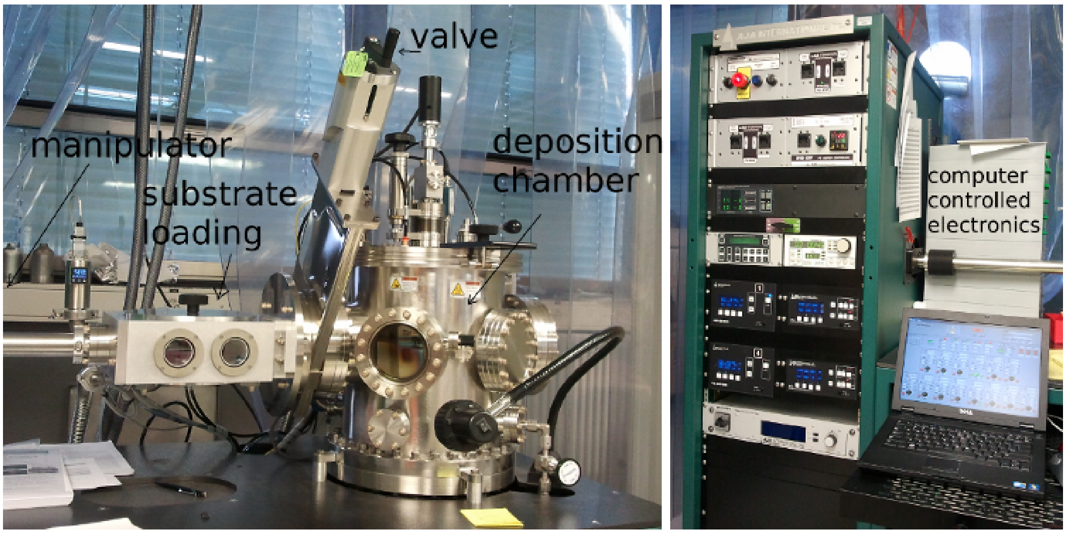

(b) AJA's Orion sputtering equipment

Figure 3.1.: Lab impressions

3.4.1. Substrate Cleaning

The ITO/glass substrates were cleaned before further usage in a an ultrasonic bath subsequently in acetone and ethanol for 5 min each. Then, the ITO/glass was cleaned with a toothbrush in 2 $vol.\%$ Hellmanex alkaline solution (H_2O-based), before ultrasonic bathing in 2 $vol.\%$ Hellmanex for 5 min. To finish, the substrates were cleaned in the ultrasonic bath for three times 5 min each in purified H_2O.

3.4.2. Sputtering of Titanium-oxide Thin-films

Titanium-oxide thin films deposited via reactive RF magnetron sputtering (see Fig.3.1b) were fabricated in the lab for thin films and photovoltaics at EMPA. Reactive refers to the reaction of the Ti-atoms in the O_2-containing plasma, to form a Ti-oxide thin-film on the substrate. One sample (EB011) was fabricated by DC-sputtering.

The varied sputtering conditions are listed in Table 3.1. Before deposition, the cleaned ITO strip was covered on the edge with a small kapton tape for direct contact with the ITO later on.

The sputtering system worked with a RF of 13.4 MHz. Before deposition, the pure solid Ti-target was cleaned 5 min in Ar plasma without O_2, then the O_2-flow was applied followed by the opening of the substrate shutter if the plasma did not break down.

Several O_2 partial pressures were applied, the O_2-content varied from 20-80%. For deposition, the power of the RF-source was kept constant at 150 W or 200 W. The total pressure in the deposition chamber during deposition was 3 mtorr ($\equiv 4 \cdot 10^{-3}$ mbar), only for sample EB009 1.5 mtorr were applied.

The substrate heater was used for samples EB006, EB008 and EB010. These samples were deposited at 200°C. Samples EB001-EB006 were solely deposited on glass substrates. Samples EB007-EB011 were deposited on both glass and ITO/glass substrates.

After deposition, the Ti-oxide substrates were stored in a vacuum-box (p=10^{-3} mbar) in the thin film lab and later in the glove-box up to 1.5 months.

3.4.3. Spin Coating

This subsection lists the recipes for spin-coated blends/solutions and the spin-coating programmes.

name	Ar [sccm]	O_2 [sccm]	O_2 [%]	p [mbar]	RF-power [W]	t [min]	temp [°C]
EB001	16	4	20	$4{\cdot}10^{-3}$	150	287,5	RT
EB002	12	8	40	$4{\cdot}10^{-3}$	150	287,5	RT
EB003	5,6	8,4	60	$4{\cdot}10^{-3}$	150	287,5	RT
EB004	2,5	10	80	$4{\cdot}10^{-3}$	150	287,5	RT
EB005	12	8	40	$4{\cdot}10^{-3}$	200	287,5	RT
EB006	12	8	40	$4{\cdot}10^{-3}$	150	287,5	200
EB007	2,5	10	80	$4{\cdot}10^{-3}$	200	180	RT
EB008	2,5	10	80	$4{\cdot}10^{-3}$	200	180	200
EB009	2,5	10	80	$2{\cdot}10^{-3}$	200	180	RT
EB010	12	8	40	$4{\cdot}10^{-3}$	200	180	200
EB011	20	3.5	15	$2.8{\cdot}10^{-3}$	200 DC	12	200

Table 3.1.: Sputtering conditions for RF magnetron sputtered TiO_2 samples (EB001-EB010). Their properties are listed in Table 4.1 in the results (sec.4.1.2).

Solaronix Titanium-dioxide Suspension

Spin coating of the Solaronix suspension did not result in homogeneous films on the substrate. With addition of a surfactant (Zonyl, similar recipe used e.g. in [38]), homogeneous film formation using spin coating was possible.

To produce the TiO_2-suspension for coating, Zonyl fluorosurfactant from Sigma was first diluted in purified water 1 : 10 by Vol. The Solaronix suspension was then mixed with the prepared Zonyl-solution 10 : 1 by Vol. to further dilute the solid content of the Zonyl to ~ 0.4 % in the TiO_2-nanoparticle suspension (TiO_2-content for usage ~ 2.7 $wt.\%$).

The H_2O-Zonyl (10:1 by Vol.)-solution is storable for several weeks when covered with aluminium foil. The Solaronix-Zonyl suspension used to spin-coat was prepared short time before deposition. For one film, approx. 250 μl suspension are required, during experiments typically 2 ml for eight substrates were fabricated.

Before deposition, the cleaned ITO/glass substrates were flushed with N_2. For filtration 0.45 μm PTFE syringe-filters were used, which were replaced after every 4^{th} film.

The Ti-nanoparticle solution was spin coated using program ETI003 with a spin-speed of 3200 rpm.

After deposition, the film was removed on the edges of the ITO-strip with a moist cotton bud (H_2O) to maintain later-on a proper contact with the ITO. The TiO_2-films were then annealed at 150 °C for 40 min on a hotplate in ambient air. The final film thickness was ~ 45 nm.

PEDOT:PSS

PEDOT:PSS from Sigma-Aldrich and Heraeus (Clevios HTL) were used as received. Since the PEDOT:PSSs were water-based, they were spin-coated outside the glove-box. Sigma-Aldrich's PEDOT:PSS was used for the standard configuration (sec.3.5.1), whereas Heraeus's PEDOT:PSS was used for the inverted configuration (sec.3.5.2).

Both PEDOT:PSS-suspensions were filtered with 5 μm PES membrane syringe filters, which were replaced after every $3^{rd} - 4^{th}$ film. Before coating, the substrates were flushed with N_2. For the standard configuration, spin program PEDOT1 (1500 rpm) was used, for the inverted configuration program ETI004 (1000 rpm) respectively.

After film coating, the edges of the substrate were cleaned from PEDOT:PSS with a moist cotton bud (H_2O) to prevent short-circuits of the cells.

The PEDOT:PSS films for the standard configuration were annealed at 125 ℃ for 15 min in ambient air, the annealing of the inverted configuration is described in sec.3.5.2.

P3HT/PCBM

For BHJ solar cells in regular and inverted geometry the recipe from [17] (2070 times cited (ISI, August 9^{th} 2012)) for the P3HT/PCBM-blend was used. The blend mixture contained 10 mg P3HT and 8 mg PCBM in 1 ml Chlorobenzene (CB) solvent. The weighing was performed in ambient air, whereas the solvent was added to the polymers in the glove-box to prevent any reactions with O_2 and H_2O. To enhance the proportion precision, typically 2 ml CB were used as basis. The mixture was then heated to 60 ℃ for 1.5 h under constant stirring on a magnet stirrer at 300 rpm. After cooling down to room temperature (3 h) the solution was ready for spin-coating. The solution could be stored in N_2-atmosphere for several weeks (up to one month) under constant stirring without affecting the cell's performance.

Before deposition, the substrate was flushed with N_2. The P3HT/PCBM blend solution was filtered each time by a new 0.45 μm PTFE membrane syringe filter, since exchanging enhanced the reproducibility of homogeneous film formation significantly. Coating program FAB700 with spin-speed 700 rpm was used to produce the P3HT/PCBM films in the glove-box.

Caynine-Dye

Cy-3 layers were produced accordingly the recipe from Dr. G. Wicht from the functional polymers lab. In the glovebox, 3.8 ml tetrafluoropropanol (TFP) were given to the previously (outside the glovebox) balanced 10 mg Cy-3. This solution is instantly usable, but was also used after six days storage under N_2-atmosphere under permanent stirring (300 rpm). The solution was filtered by a new 0.45 μm PTFE membrane syringe filter for each film. Spin program DHP4000 with spin-speed of 4000 rpm was used to produce the cyanine-layers in the glove-box.

Spin-Coating Programmes

name		time [s]	ramp [rpm/s]	speed [rpm]
PCB-diyne (used in sec.3.5.3)	step 1	2	3000	200
	step 2	60	3000	500-2000
FAB700 (for P3HT/PCBM)	step 1	60	3000	700
	step 2	0	100	0
DHP4000 (for Cyanine-Dye Cy-3 sec.3.5.3)	step 1	3	3000	300
	step 2	60	3000	4000
PEDOT1 (for Sigma's PEDOT:PSS) [standard configuration sec.3.5.1]	step 1	30	0	0
	step 2	30	1000	400
	step 3	60	1000	1500
ETI003 (for Solaronix TiO_2)	step 1	10	0	0
	step 2	10	400	400
	step 3	60	1000	3200
ETI004 (for Heraeus's PEDOT:PSS) [inverted configuration sec.3.5.2]	step 1	10	0	0
	step 2	30	1000	400
	step 3	60	1000	1000

Table 3.2.: Relevant spin-coating programmes

3.4.4. Thermal Vapor Deposition

The deposition chamber is incorporated in the glove-box to prevent any oxidation during and after the depositions. All depositions were performed in high vacuum in the $\sim 5 \cdot 10^{-6}$ $mbar$ range. The needed heating currents through the boat source for evaporation varied from $25-55$ amperes depending on the target deposition material. Metal top contacts (Al,Au,Ag) were deposited through a solar cell mask, which defined the final design of the eight single solar cells on the common substrate sample (see Fig.3.3). Interlayers (MoO_3,C_{60}) were deposited under an edge-shielding mask, to prevent deposition at three of the four substrate edges (proportions shown in Fig.3.3b). Heating rate was $\sim$ 10 $A/10min$. Substrate rotation was set to 2 rpm. Tab.3.3 lists the parameters for thickness and deposition rate control for every target material.

target	ρ $[g/cm^3]$	z-ratio	tooling-factor [%]
Ag	10.5	0.529	62
Al	2.7	1.08	79.1
Au	19.3	0.381	62
C_{60}	1.72	1	63.8
MoO_3	4.7	1	90

Table 3.3.: Used parameters for thickness measurements

Molybdenum-oxide

MoO_3 powder was evaporated from a Mo source boat with a heating current of ~ 55 A at a constant rate of 0.2 $\mathring{A}/s$.

Fullerene

C_{60} molecules (powder) were evaporated from a folded tantalum source boat with circular openings in the corresponding tantalum cover at a rate of 0.1 $\mathring{A}/s$ for the first 5 nm and 0.2 $\mathring{A}/s$ for the rest of the deposition. Current needed was ~ 45 A.

Aluminium

Al pellets were evaporated from a tungsten source boat. To start the evaporation of Al, ~ 35 A were needed. Then the current had to be reduced to ~ 28 A to maintain a rate of 0.2 $\mathring{A}/s$ for the first 10 nm. The current was enhanced to reach a rate of 0.6 $\mathring{A}/s$ for the remaining Al-layer. During deposition the building of an Al/W-alloy by the Al-target with the W-boat caused sometimes problems, as well as the deposition rates were sometimes difficult to control. A glowing of the Al target was identified.

Silver

Ag-pellets were evaporated from a tungsten source boat. A current of ~ 25 A was required for the deposition of the first 10 nm at a rate of 0.2 $\mathring{A}/s$, the remaining Ag was deposited at 0.6 $\mathring{A}/s$. Ag deposition was more stable compared to Al, the heating current was only slightly enhanced to reach the final deposition rate.

Gold

A tungsten source boat was used, the heating current was $\sim 42\ A$. A strong glowing of the target was determined. The deposition rate was 0.2 $\AA/s$ for the first 10 nm and 0.6 $\AA/s$ for the remaining film thickness.

3.5. Cell Fabrication

This section summarizes the produced cells in terms of layer composition and the corresponding layer thicknesses. Three different configurations of organic solar cells were fabricated:

1. Standard configuration P3HT/PCBM, sec. 3.5.1
2. Inverted configuration P3HT/PCBM, sec.3.5.2
3. Inverted configuration Cy-3, sec.3.5.3

The basic compositions of these three fabricated cell configurations are shown in Fig.3.2.

The standard configuration is also known as regular or superstrate geometry, whereas the inverted architecture is sometimes referred as substrate configuration. This is not exactly true in this case, since in every geometry the light passes through the substrate (glass) and is blocked at the top metal contact. Regarding the light-path, each geometry has superstrate architecture. The inverted configuration refers solely to the opposite electrode-configuration regarding the incident light-path.

Two configurations (standard and inverted) have the P3HT/PCBM-blend as the active absorption layer (BHJ), whereas the second inverted configuration has a separated thin film cyanine-dye (Cy-3) on a C_{60} layer as an active absorption layer (planar HJ).

The layer deposition order is from the bottom ITO electrode to the top, where a metal electrode is deposited. For the regular configuration the ITO is the positive electrode. A solar cell is considered to be inverted, if the bottom electrode is negative (Fig.3.2). The simplest structure regarding the number of depositions is the standard type with three, followed by the inverted P3HT configuration with four and the inverted Cy-3 configuration with five deposited layers on the ITO/glass substrate.

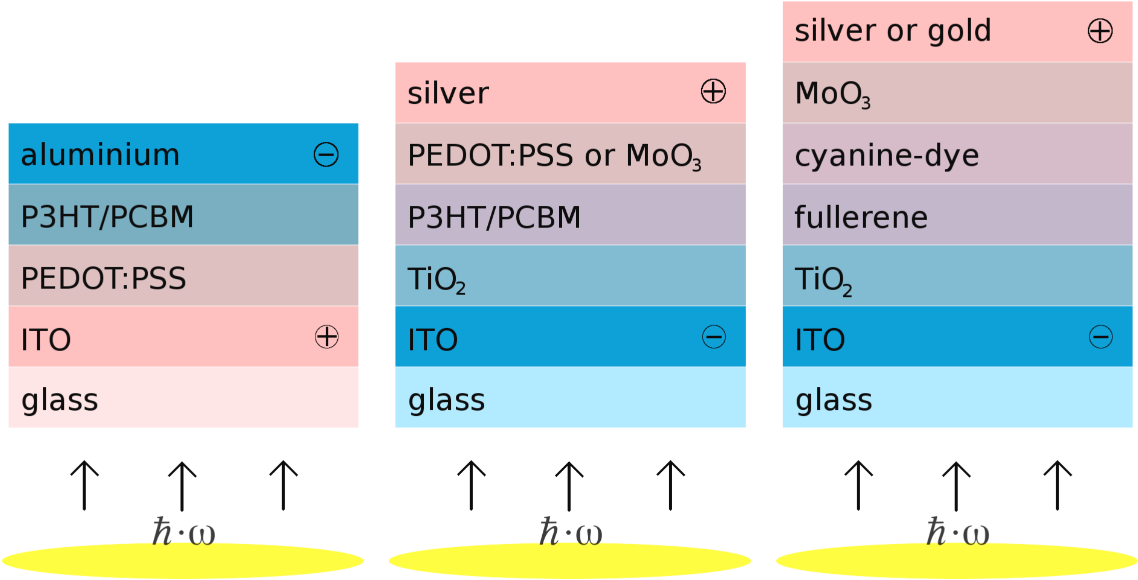

(a) Standard P3HT/PCBM configuration

(b) Inverted P3HT/PCBM configuration

(c) Inverted Cy-3 configuration

Figure 3.2.: Layer order of the three fabricated configurations. Depositions were realised from the bottom ITO substrate to the top metal electrode. The inverted structure has opposite charged electrodes compared to the standard configuration with regard to the incident light-path.

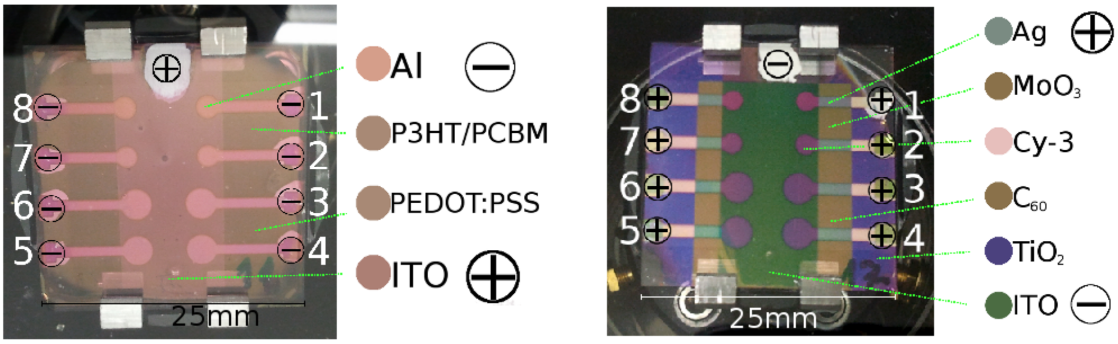

(a) Standard P3HT/PCBM sample 11.

(b) Inverted Cy-3 substrate sample 17.

Figure 3.3.: Top view on two finished solar cells mounted on the sample holder. The central ITO-strip over the glass substrate is the bottom electrode for all eight solar cells of the corresponding sample (indicated from 1-8). The top metal electrodes are evaporated as final deposition (sec.3.4.4). The small solar cells (circles on ITO-strip, connected by the metal-fingers to pins nr.1,2,7,8) include each an active area of 3.1 mm^2, the large solar cells (nr.3-6) cover 7.1 mm^2 each. Silver-paste was deposited on the contact pins to enhance electrical contact with the $35 - 60\ nm$ thick metal-fingers and the ITO.

3.5.1. Standard Configuration Cells based on P3HT/PCBM-blend

To start, an established recipe for P3HT/PCBM BHJ solar cells was used [17], also referred as the standard P3HT/PCBM configuration. However, first samples showed only poor performance (see sec.4.2.1). The efficiency could be enhanced to reasonable values during the fabrication of total 14 samples of this type.

14 ITO/glass substrates were similarly coated with $\sim$ 65 nm PEDOT:PSS (Sigma) in ambient air (see sec.3.4.3). Henceforth, the substrates were kept and proceeded under N_2-atmosphere in the glove-box. The $\sim$ 100 nm thick P3HT/PCBM layer was then spin-coated on the PEDOT:PSS. Only on the first two samples 100 nm thick Al electrodes were evaporated, the following 12 samples were coated by 35 nm thick Al electrodes. After Al-deposition the samples were annealed at 150°C for 30 min. To improve the contact of the sample-holder's pins with the solar cell's electrodes, each metal-finger end was coated with Ag-paint. For the ITO-contact pin, the PEDOT:PSS and P3HT/PCBM films were locally removed with a solvent (CB) moist cotton bud before deposition of the Ag-paint. After 20 min, the solvents of the Ag-paint had dried and the cells could be measured. Samples were stored in the dark (covered with Al-foil) under N_2-atmosphere.

The initial performances are given in Table 4.2 in the result section.

3.5.2. Inverted Configuration Cells Based on P3HT/PCBM-blend

After P3HT/PCBM samples with accurate efficiencies could be fabricated in the regular geometry, its inverted configuration was developed. Inverted P3HT/PCBM geometries are reported amongst others in [24][25][26][28][38].

To summarize the 19 inverted P3HT/PCBM samples, table 3.4 shows each sample configuration.

As additional layer compared with the standard geometry, the electron collecting TiO_2 layer was first deposited on the ITO, either via spin-coating (sec.3.4.3, samples P3HT$_{inv}$01-08,10,14,16-19) or via sputtering (sec.3.4.2, samples P3HT$_{inv}$09,11,13,15). Fabricated TiO_2-substrates were stored in the glove-box up to 1.5 months. Spin-coated TiO_2 was $\sim$ 45 nm thick, sputtered thin films varied from $\sim$ $35 - 40$ nm (see Tab.4.1). On the TiO_2 the $\sim$ 100 nm P3HT/PCBM-blend was coated similarly to the regular geometry.

To deposit the hole-collecting PEDOT:PSS (Heraeus) on the P3HT/PCBM (sec3.4.3), the samples were taken out of the glove-box. Only after surface activation of the P3HT/PCBM thin-film with a 10 s UV-ozone flash, a homogeneous $\sim$ 100 nm thick PEDOT:PSS film formed, which visually dried in ambient air shortly after deposition. The samples were then rapidly returned into N_2-atmosphere.

Alternatively to PEDOT:PSS, a $10-30$ nm thick MoO_3 layer was evaporated (sec.3.4.4).

After deposition of the top Ag contact electrode ($35-60$ nm), the samples were annealed for 30 min at 150°C if not indicated differently. Annealing procedure is discussed in sec.4.2.2.

Then every metal-finger contact was coated with Ag-paint. For the ITO-contact pin, the PEDOT:PSS and P3HT/PCBM films were locally removed with a solvent (CB) moist cotton bud before Ag-painting. Samples were stored in the dark (covered with Al-foil) under N_2-atmosphere.

name	Ti-oxide	P3HT	PEDOT:PSS	MoO_3	Ag
P3HT$_{inv}$01	Solaronix		Sigma(mod.)	-	-
P3HT$_{inv}$02	Solaronix		Sigma(mod.)	-	35 nm
P3HT$_{inv}$03	Solaronix		Sigma(mod.)	-	35 nm
P3HT$_{inv}$04	Solaronix		Sigma(mod.)	-	35 nm
P3HT$_{inv}$05	Solaronix		Heraeus	-	35 nm
P3HT$_{inv}$06	Solaronix		Heraeus	-	35 nm
P3HT$_{inv}$07	Solaronix		Heraeus	-	35 nm
P3HT$_{inv}$08	Solaronix		Heraeus	-	35 nm
P3HT$_{inv}$09	EB007		Heraeus	-	35 nm
P3HT$_{inv}$10	Solaronix		Heraeus	-	35 nm
P3HT$_{inv}$11	EB008		Heraeus	-	35 nm
P3HT$_{inv}$12	Solaronix		Heraeus	-	$25+35$ nm
P3HT$_{inv}$13	EB009		Heraeus	-	$25+35$ nm
P3HT$_{inv}$14	Solaronix		-	20 nm	$25+35$ nm
P3HT$_{inv}$15	EB009		-	20 nm	$25+35$ nm
P3HT$_{inv}$16	Solaronix		-	10 nm	60 nm
P3HT$_{inv}$17	Solaronix		-	20 nm	60 nm
P3HT$_{inv}$18	Solaronix		-	30 nm	60 nm
P3HT$_{inv}$19	Solaronix		Heraeus	-	60 nm

Table 3.4.: List of inverted P3HT/PCBM samples. For initial performances, see Table 4.3.

3.5.3. Inverted Solar Cells Based on Cyanine/C$_{60}$ Bilayer

With the knowledge about the working principle, inverted Cy-3 solar cells were fabricated. Table 3.5 summarizes the 21 fabricated samples. During this thesis, in [39] a cyanine dye incorporated into an inverted organic solar cell was reported for the first time.

On the Ti-oxide coated substrates an electron accepting layer based on fullerene was deposited. Layer thickness of thermal evaporated C_{60} (sec.3.4.4) was varied from $40-80$ nm.

The PCB-diyne (a cross-linkable derivative of PCBM, provided by Eric Wimmer) thickness was varied during spin-coating (programme see Tab.3.2: Cy-3_{inv}05: 500 *rpm*, 06: 1000 *rpm*, 07: 1000 *rpm* and 08: 2000 *rpm*). The coated suspension contained 10.3 *mg* PCB-diyne and 0.3 *mg* Cy-3 in 1 *ml* CB. After coating, the PCB-diyne films were annealed at 135°C for 3.5 *h* on a hotplate in the glove-box to initiate polymerization.

On the fullerene, a $\sim$ 16 *nm* Cy-3 layer was spin-coated as described in sec.3.4.3. The PCB-dyine samples (Cy-3_{inv}05-08) were similarly coated with program DHP4000 (Tab.3.2), but the suspension was based on 10 *mg* Cy-3 in 2.5 *ml* CB instead of typically used 3.8 *ml* TFP. The Cy-3 films of Cy-3_{inv}18,20 and 21 were treated by a 10 *s* UV-ozone flash outside the glove-box, before the MoO_3 and contact electrode were deposited.

Thermally evaporated MoO_3 thickness was varied from $5-30$ *nm*.
On all samples a 60 *nm* thick silver electrode was deposited, but for Cy-3_{inv}19 and 21 gold was used.

The contacts were prepared with *Ag*-paint after Cy-3 remainings on the ITO were locally removed by a moist (CB) cotton bud.

3.6. Measurement Parameters and Analysis

3.6.1. Atomic Force Microscopy

The AFM from Nanosurf was used with delivered software. Before each scan, the amplitude and the phase-shift of the cantilever were re-setted. All scans were recorded using two different cantilevers with $f_{res} = 162\ kHz$ resp. $f_{res} = 165\ kHz$.

Used gains: P:500, I:1500, D:0
AFM images were processed using `Gwyddion` (GNU). Polynomial background subtraction (3^{th} grade in x- and y-direction) was followed by line correction based on the alignment of the height median. Last step was correction of horizontal error lines. Presented AFM roughness values were derived by averaging four scans of every sample with different areas of $2 \cdot 2\mu m^2$ and $8 \cdot 8\mu m^2$ or $32 \cdot 32\mu m^2$.

3.6.2. Solar Cell Performance

Samples were mounted in the glove-box on an air-tight sample holder. The solar simulator had a light intensity of $\sim$ 90 mW/cm^2 under an AM1.5 filter set. Cells were measured from -0.5 to 1.0V under light irradiation and values were normalized to 100 mW/cm^2 by the

name	Ti-oxide	fullerene	Cy-3	MoO_3	Ag
Cy-3$_{inv}$01	Solaronix	80 nm C_{60}		5 nm	60 nm
Cy-3$_{inv}$02	Solaronix	80 nm C_{60}		20 nm	60 nm
Cy-3$_{inv}$03	EB008	80 nm C_{60}		5 nm	60 nm
Cy-3$_{inv}$04	EB008	80 nm C_{60}		20 nm	60 nm
Cy-3$_{inv}$05	Solaronix	PCB-diyne		20 nm	60 nm
Cy-3$_{inv}$06	Solaronix	PCB-diyne		20 nm	60 nm
Cy-3$_{inv}$07	EB010	PCB-diyne		20 nm	60 nm
Cy-3$_{inv}$08	EB010	PCB-diyne		20 nm	60 nm
Cy-3$_{inv}$09	EB008	40 nm C_{60}		20 nm	60 nm
Cy-3$_{inv}$10	EB008	60 nm C_{60}		20 nm	60 nm
Cy-3$_{inv}$11	EB010	40 nm C_{60}		10 nm	60 nm
Cy-3$_{inv}$12	EB010	40 nm C_{60}		20 nm	60 nm
Cy-3$_{inv}$13	EB010	40 nm C_{60}		30 nm	60 nm
Cy-3$_{inv}$14	EB007	40 nm C_{60}		30 nm	60 nm
Cy-3$_{inv}$15	EB008	40 nm C_{60}		30 nm	60 nm
Cy-3$_{inv}$16	EB009	40 nm C_{60}		30 nm	60 nm
Cy-3$_{inv}$17	EB011	40 nm C_{60}		30 nm	60 nm
Cy-3$_{inv}$18	EB008	40 nm C_{60}		30 nm	60 nm
Cy-3$_{inv}$19	EB008	40 nm C_{60}		30 nm	60 nm Au
Cy-3$_{inv}$20	EB008(n)	40 nm C_{60}		30 nm	60 nm
Cy-3$_{inv}$21	EB010(n)	40 nm C_{60}		30 nm	60 nm Au

Table 3.5.: List of inverted Cy-3 samples. For initial performances, see Table 4.4.

software. The diode properties were subsequently measured in the dark from -1.5 to 1.5V.

The eight solar cells were measured individually. On many samples, one or several cells did not work for different reasons. Presented results for initial performances are the averaged values of the three best cells of every sample. Data presentation was done with `Origin` and `Openoffice` (GNU).

3.6.3. Profilometer

To obtain height-profiles, a profilometer from Ambios was used under its XP2 software. The thicknesses were measured over scratches, either applied with a scalpel (soft polymers) or by lifting off a small kapton tape strip (sputtered TiO_2). The scratches were scanned both from high-to-low and low-to-high terasses, and then levelled. To obtain the height, only smooth straight profiles with a minimum length of 300μm were used for characterization. Three low-to-high and three high-to-low profiles were averaged.

3.6.4. Pictures

Pictures were recorded by a 5 Mpx camera integrated in the Samsung Galaxy I (GTI-9000) smartphone. Processing included only brightness and contrast adjustments. Layering of image-planes were done with `GIMP` (GNU). Exception is the image on the titlepage, where more effects were applied.

3.6.5. Sheet-Resistance Measurements

Sheet-resistances were measured by 4-probe measurements. The linear 4-probe head was connected to the Keithley 2400, which was used as current source between the two outer pins. Using 4-probe measurement, the voltage between the inner two pins was measured. The resistance was measured during three different applied currents to verify resistance linearity on three different spots on the sample. Different means the current was at least more than doubled, usually several magnitudes of different currents confirmed the resistance's linearity. The sample's sheet-resistance was calculated by Ohm's law ($\Omega = U/I$) multiplied for a linear probe array by the factor $\frac{2\pi}{ln(4)} = 4.53$ ([40][41]) to obtain the sheet-resistance in $\Omega/\Box$. Nine obtained sheet-resistances for one sample were averaged.

3.6.6. Ultraviolet-Visible Absorption

UV-Vis absorption was measured from $200 - 800$ nm with a scan speed of 10 nm/s. The spectrometer takes the attenuation of the sample as its absorption, which may not always be correct (light-scattering at interfaces, interferences, etc.). For every scan, first a blank sample was scanned. Then the film of interest, deposited on the equivalent blank, was scanned. The difference in absorption of these curves is shown as the absorption spectrum of the film, data processing was done in `Origin`. Similar results for the absorption were confirmed by the automatic baseline absorption function of the software.

3.6.7. X-Ray Diffractometer

Two different X-ray diffractometers (XRD) were used (sec.3.2). Since the Bruker setup was available for students, most of the scans were performed on the Bruker Kristalloflex. The first scans were obtained with the Panalytical X'Pert. To compare measurements, every plot was normalized to counts per second (cps).

All TiO_2-films on ITO were measured with the Bruker XRD, which provided a Cu-K_α wavelength of 1.54 $\AA$.

Since the sputtered TiO_2 films were only $\sim 40\ nm$ thin, a typical $\theta - 2\theta$ setup would and did not show x-ray diffraction patterns of the films. The x-ray penetrated too much into the amorphous substrate glass, as a result there were no diffraction patterns. Therefore the incident angle of the x-ray beam on the sample was chosen at constant small angle $\theta = 1.0°$ (sometimes referred as ω) and only the moving sensor scans the angle 2θ. This scan method analyses only the very top surface of a sample (usable e.g. for thin films) and is referred as grazing incident XRD (GIXRD). The sensor (2θ) scan was chosen from $20° - 30°$, since both anatase and rutile phases of TiO_2 have the main crystallographic peak in this range.

To reduce noise and receive enough signals, long term measurements were performed. Step increment was 0.05°, integration time 180 s per step (gives a total scan time of 10 h for the 10°-scan). A divergence slit of 0.2 mm was mounted. A 60 μm Ni-foil filtered the Cu-K_β ($\lambda = 1.39\ \mathring{A}$) radiation to below 1% of the Cu-K_α x-rays.

Obtained data was processed using `Origin`.

4. Results

4.1. Single Thin-film Analysis

To understand the interplay of the individual layers which build up the organic solar cell, this section characterizes single layers.

4.1.1. Indium Tin Oxide

ITO substrates were investigated after the cleaning procedure (sec.3.4.1) by AFM and compared with a rinsed ITO sample. Fig.4.1 shows the cleaned surface, on which ITO grain boundaries can be identified. Several holes in Fig.4.1a indicate the bombardment during ultrasonic bath. Averaged RMS surface roughness was 0.55 nm. Solely rinsed ITO had a RMS roughness of 0.28 nm and the grains were not visible. Sheet-resistance remained constant at $20\Omega/\square$.

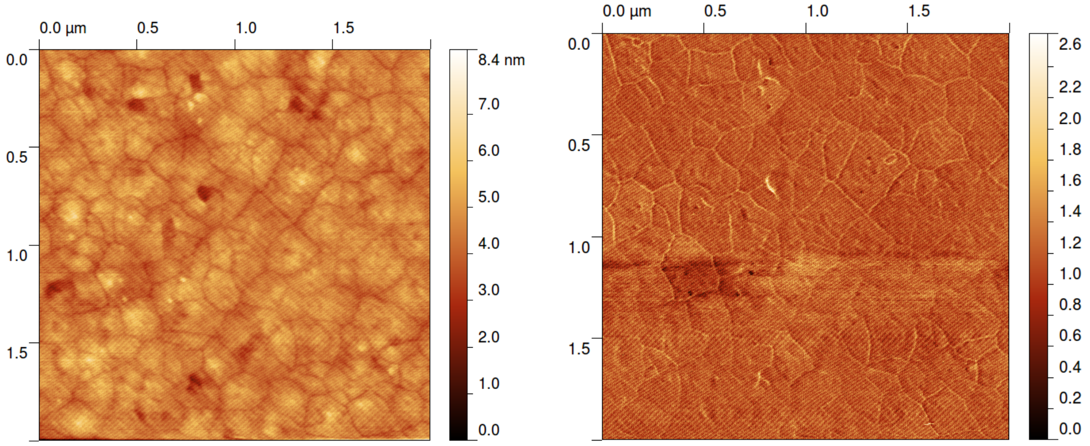

(a) ITO after cleaning, topography. RMS surface roughness: 0.51 nm

(b) ITO after cleaning, phase

Figure 4.1.: AFM image of ITO, which was cleaned for 30 min in ultrasonic bath and brushed with a toothbrush.

4.1.2. Titanium-oxides

The Ti-oxide thin films were analysed using GIXRD, UV-Vis and the AFM. Thicknesses were measured with the profilometer and the sheet-resistances with a 4-probe scan head (sec.3.6.5). All samples showed high sheet-resistances in the GΩ/□-range. With the used 4-probe setup, exact determination was not possible (high accuracy up to 200MΩ, given in specifications). To summarize, Table 4.1 lists the results. Regarding the phase, small crystallization is indicated with "phase−−" for indicated, going to "phase" for recognizable and "phase++" for high crystallinity.

name	O_2 [%]	Temp (°C)	power	h [nm]	RMS roughness	phase on glass	phase on ITO
EB001	20	RT	150	48	-	amorph	-
EB002	40	RT	150	32	-	amorph	-
EB003	60	RT	150	35	-	anatase–	-
EB004	80	RT	150	32	-	ana–, rut– –	-
EB005	40	RT	200	69	-	ana–, rut–	-
EB006	40	200	150	46	-	anatase	-
EB007	80	RT	200	39	$\sim 0.5\ nm$	amorph	ana– –, rut– –
EB008	80	200	200	40	$\sim 0.7\ nm$	anatase+	anatase++
EB009	80	RT	200	35	$\sim 2.7\ nm$	amorph	rutile–
EB010	40	200	200	37	$\sim 0.6\ nm$	-	anatase++
EB011	15	200	200 DC	110	$\sim 7.3\ nm$	rutile++	rutile++

Table 4.1.: Properties of sputtered Ti-oxides. Sputtering conditions are listed in Table 3.1.

Following literature ([31] [32]), first TiO_2 thin films were deposited on glass. These were mostly amorphous. The 4^{th} sample (EB004, 80% O_2) had small crystallization, compared to first samples (EB001-003) with lower O_2 content in the Ar-plasma. Crystallization to anatase phase was obtained by heating the substrate to 200°C during deposition. After the 6^{th} run, the TiO_2 thin films were deposited on glass and on ITO, to produce solar cells and analyse the films simultaneously. Because the deposition rate was slow, the RF power was enhanced from $150W$ to $200W$, which reduced the deposition time for a $\sim 40\ nm$ thin-film from 4.8h to 3h. The films fabricated during the same run on different substrates (glass or ITO) were not equal regarding x-ray diffraction (see Fig.4.2a) and UV-Vis absorption (Fig.4.5a). The films deposited on ITO had stronger crystallization than films deposited on glass. This can be identified in Fig.4.2a, where the anatase phase peak of EB008 (deposited at 200°C) is more pronounced on ITO than on glass. EB009 on glass is amorphous, whereas EB009 in ITO shows a small rutile peak.

To obtain rutile phase, high O_2 content and low total pressure were chosen at room temperature (EB009) [32]. This did not lead to a high crystalline rutile phase. But sample EB011, sputtered with DC conditions instead of RF-magnetron sputtering, showed rutile phase (Fig.4.2b), and was thick (110 nm) compared to the other TiO_2 thin films (~ 40 nm). The Solaronix TiO_2 film showed its claimed anatase character, but the peak was rather wide and less pronounced, meaning the anatase crystals were rather small compared with the sputtered anatase thin films (Fig.4.2b).

RMS surface roughness was measured by AFM. The $8 \cdot 8 \mu m^2$ scans of the Solaronix and sputtered anatase films are shown in Fig.4.3. Solaronix TiO_2 films (sec.3.4.3) had a high RMS roughness of 11.5 nm compared with the sputtered anatase Ti-oxides, which had a RMS roughness below 1 nm. The rough surface of the Solaronix film could be attributed to the suspension, which contained TiO_2 anatase nanoparticles with a diameter of ~ 9 nm.

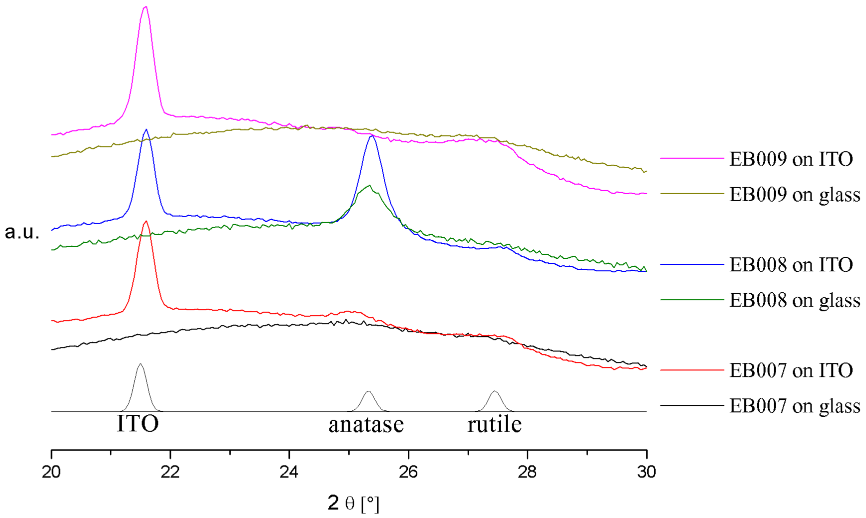

(a) Substrate comparison

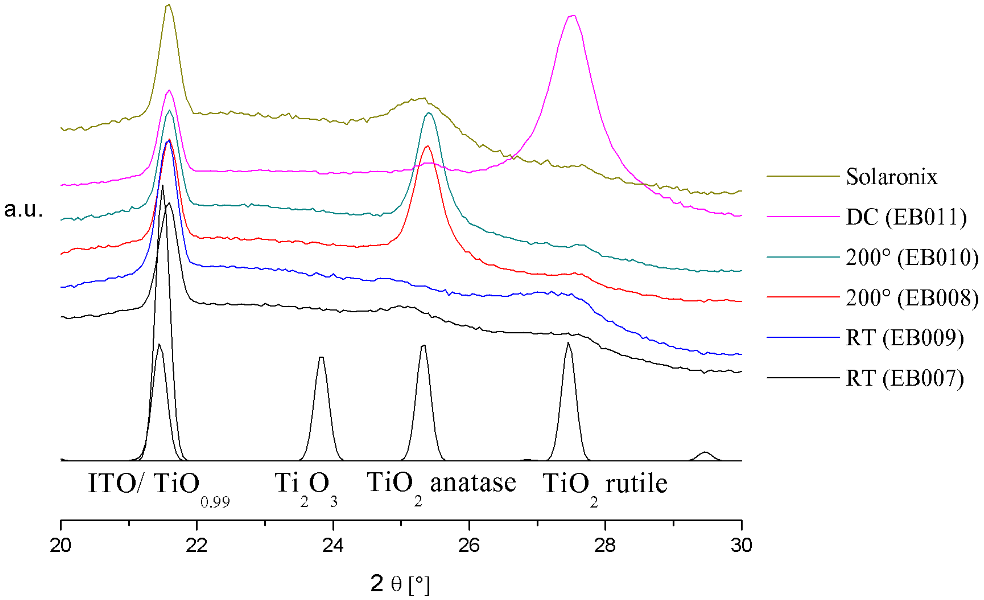

(b) All TiO_2 thin-films on ITO.

Figure 4.2.: GIXRD measurements of the different TiO_2 thin-films.

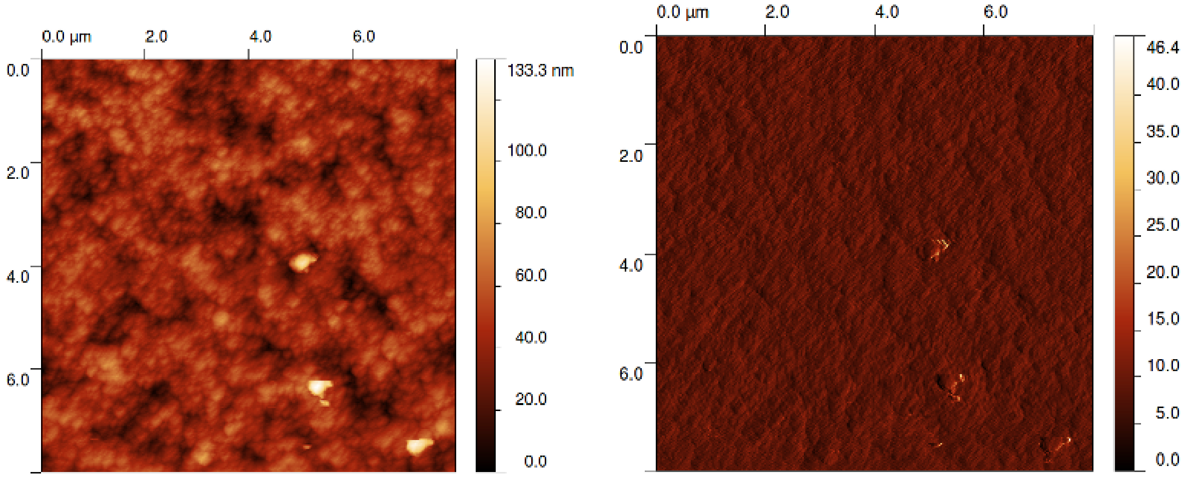

(a) Solaronix, topography.
RMS surface roughness: 11.5 *nm*

(b) Solaronix, phase

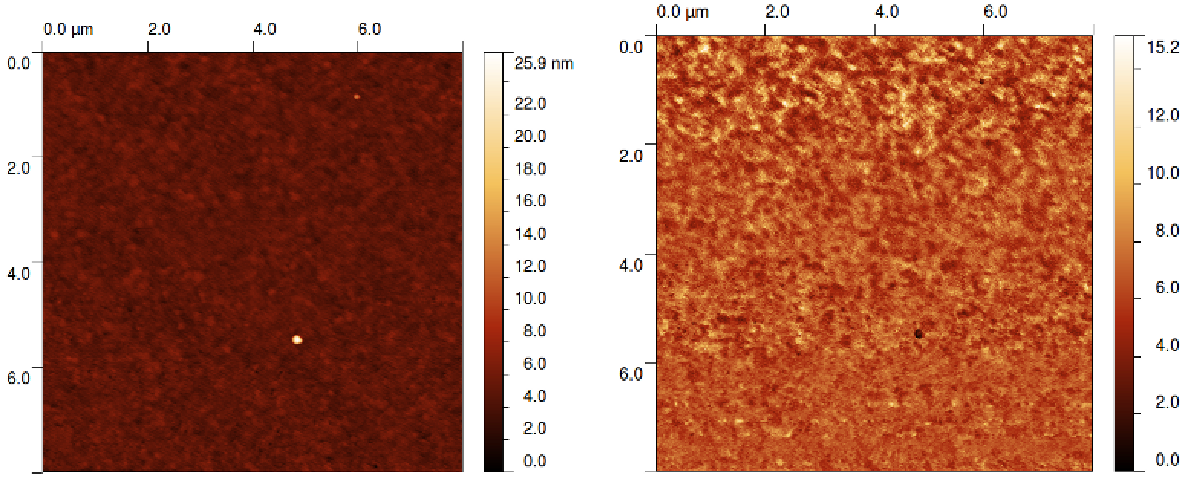

(c) EB008, topography.
RMS surface roughness: 0.7 *nm*

(d) EB008, phase

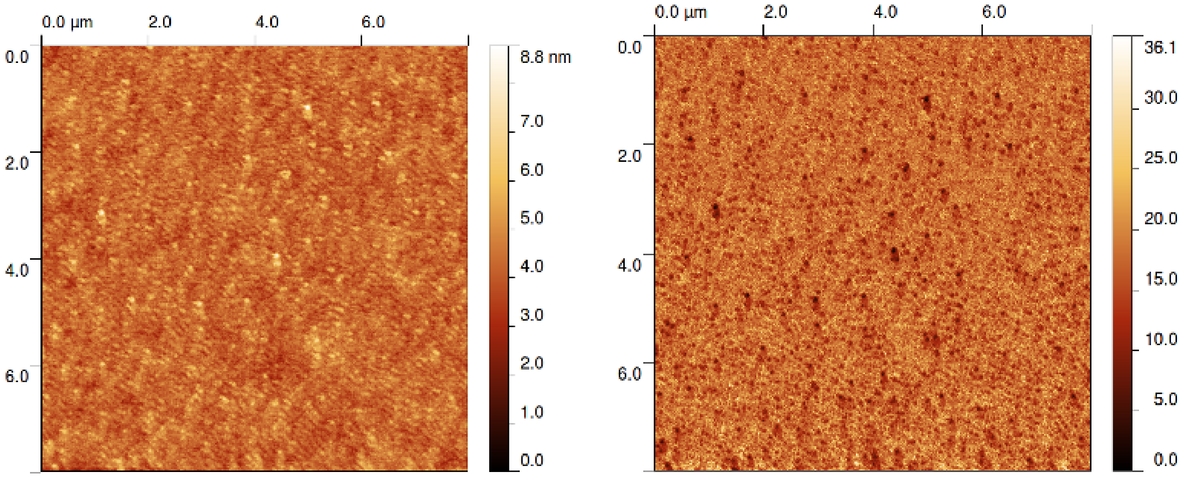

(e) EB010, topography.
RMS surface roughness: 0.6 *nm*

(f) EB010, phase

Figure 4.3.: AFM images of anatase phase TiO_2

Sputtered rutile containing TiO_2 films had higher surface roughnesses than sputtered anatase films. In Fig.4.4, $8 \cdot 8 \mu m^2$ rutile containing TiO_2 AFM scans are shown. Individual spikes in Fig.4.4a are ~ 20 nm high, the DC sputtered rutile sample (EB011) showed up to 70 nm high spikes.

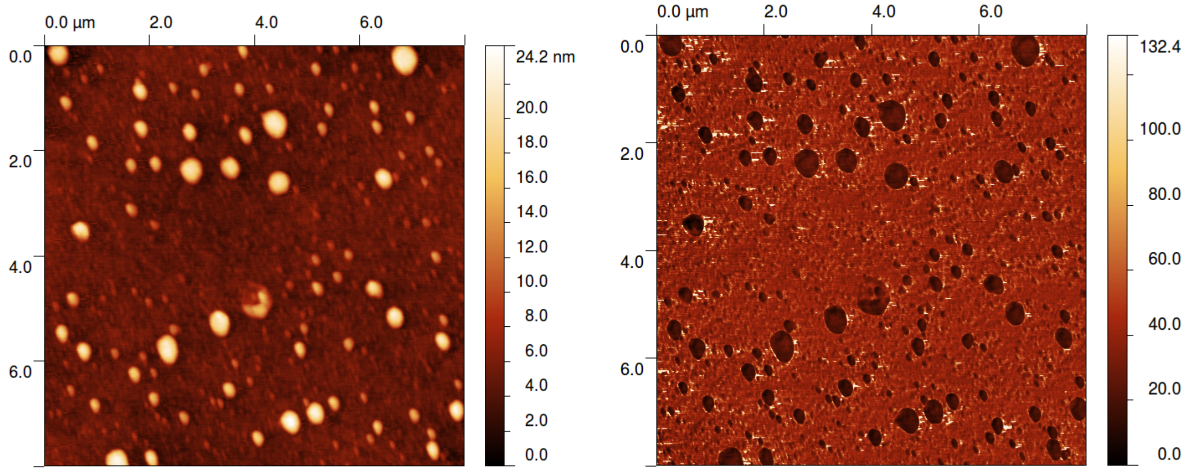

(a) EB009, topography.
RMS surface roughness: 2.7 nm

(b) EB009, phase

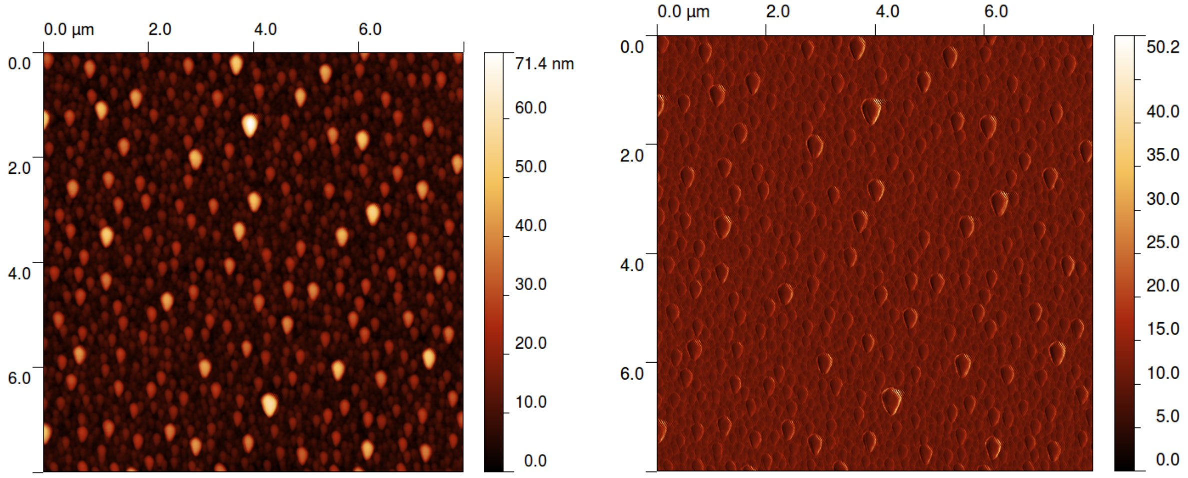

(c) EB011, topography.
RMS surface roughness: 7.3 nm

(d) EB011, phase

Figure 4.4.: AFM images of rutile phase TiO_2

The UV-Vis absorption of the thin films on ITO are shown in Fig.4.5b. The Solaronix film is the most transparent, the 110 nm thick rutile (EB011) film absorbs already $\sim 40\%$ of the incident light. As can be seen in Fig.4.5a, the sputtered TiO_2 films have on ITO a hump at $\sim$ 500 nm and absorb $\sim$ 18% of the incoming light. Towards the band-gap of the Ti-oxide ($\sim$ 400 nm), the absorption decreases to $\sim$ 0 before the light is absorbed completely. The theoretical band gap of anatase is 3.2 $eV \equiv 388$ nm, and the gap for rutile is slightly smaller at 3.0 $eV \equiv 414$ nm. The trend from anatase (Solaronix) to rutile (EB011) is shown in Fig.4.5b, although the spectra for the Solaronix starts its absorption at $\sim$ 350 nm and EB011 at $\sim$ 400 nm.

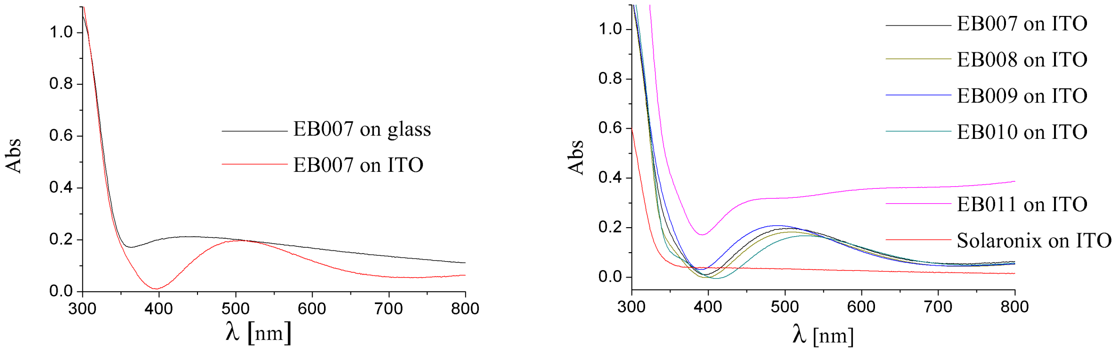

(a) Substrate comparison of amorphous EB007 on glass and ITO

(b) TiO_2 films on ITO. Solaronix (anatase, $\sim$ 45 nm) and EB011 (rutile, $\sim$ 110 nm) are the edge cases.

Figure 4.5.: UV-Vis absorption spectra of sputtered TiO_2.

4.1.3. Molybdenum-oxide

The deposited MoO_3 (sec.3.4.4) had a high sheet-resistivity in the G$\Omega/\square$ range. Its transparency in the visible spectrum down to $\sim$ 400 nm is shown in Fig.4.7d. The surface of 30 nm MoO_3 deposited on glass had a RMS roughness of 0.9 nm (Fig.4.6a).

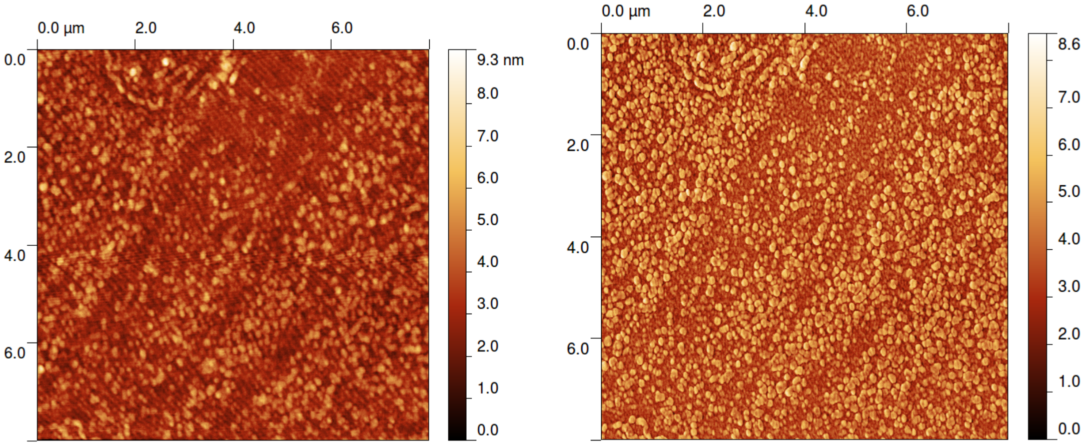

(a) MoO_3, topography.
RMS surface roughness: 0.9 nm

(b) MoO_3, phase

Figure 4.6.: $8 \cdot 8 \mu m^2$ AFM scan of a thermally evaporated 30 nm MoO_3 layer on glass.

4.1.4. Cyanine-Dye

Cy-3 layer was analysed using UV-Vis. The absorption spectrum of a Cy-3 film on C_{60} is shown in Fig.4.7a. Absorption maximum is at $\lambda = 577$ nm with 15.6%. With this absorption, the Cy-3 layer thickness was determined to ~ 16 nm. The strongly red coloured dye-solution absorbs most photons in the yellow light spectrum.

4.1.5. P3HT/PCBM

The P3HT/PCBM layers were analysed with UV-Vis and the profilometer. The thickness of the film was ~ 100 nm, measured on glass, confirmed on PEDOT:PSS and on Solaronix TiO_2. The absorption spectra of the initial films and after thermal annealing at 150°C for 30 min are shown in Fig.4.7c for the inverted and the standard geometry. The inverted architecture absorbs less than the standard from 800 to 600 nm. The inverted P3HT/PCBM film was deposited on Solaronix TiO_2, the standard on a PEDOT:PSS (Sigma) substrate. After annealing, the absorption was enhanced at $\lambda = 500$ nm for both cases to $\sim 50\%$.

4.1.6. PEDOT:PSS

Sheet-resistivity measurements were performed on standard configuration PEDOT:PSS (Sigma) layers.

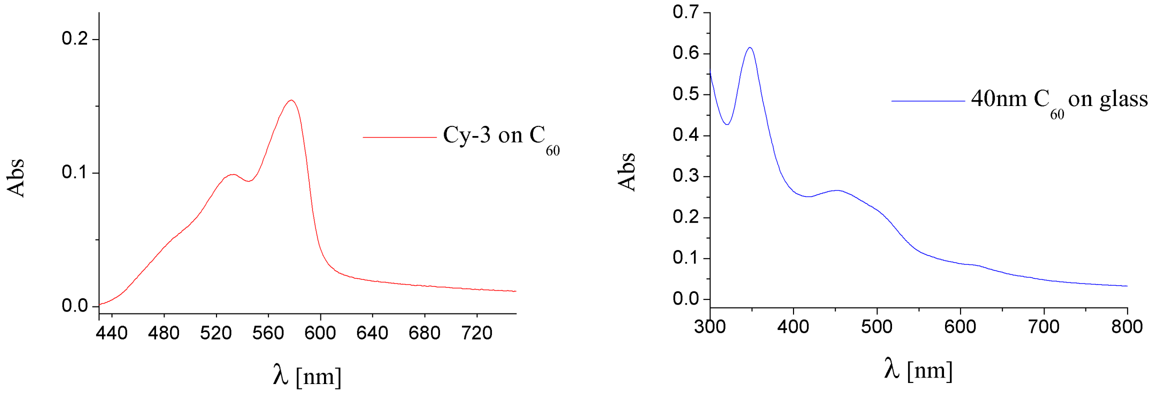

(a) UV-Vis absorption of Cy-3 (b) UV-Vis absorption of 40 nm C_{60}

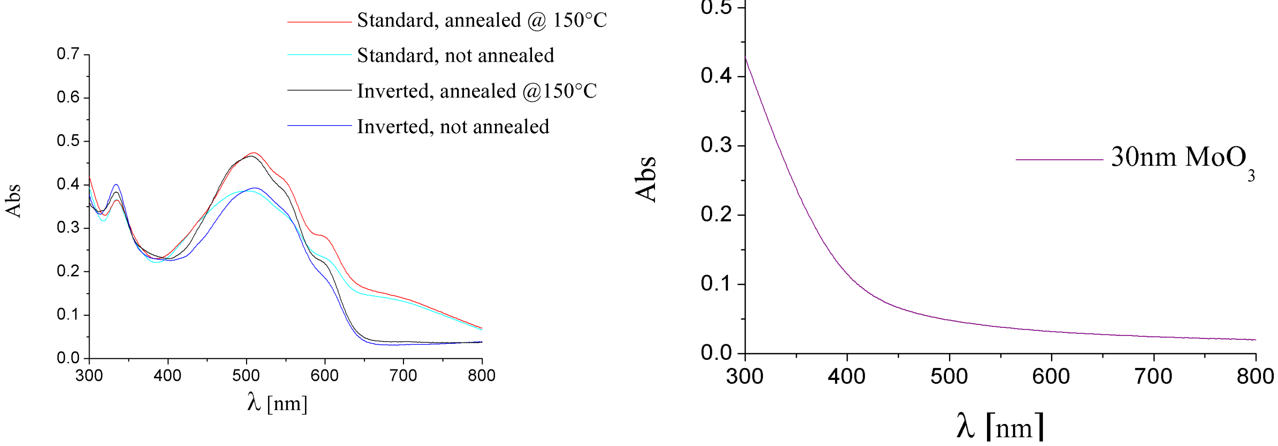

(c) UV-Vis absorption of P3HT/PCBM (d) UV-Vis absorption of 30 nm MoO_3

Figure 4.7.: UV-Vis absorptions of different films.

After a new syringe filter, the first coated PEDOT:PSS film was ~ 65 nm high and had a resistivity of ~ 100 kΩ/□. The 3^{rd} film coated with the same syringe filter was ~ 55 nm high and had a resistivity of ~ 150 kΩ/□. This could be explained with a clogging of the filter. The conductivity depends not linear on the thickness. 85% of the PEDOT:PSS thickness delivered 66% of the initial conductivity. This experiment was repeated and the results confirmed.

For the inverted geometry, PEDOT:PSS in aqueous solution was coated on the hydrophobic P3HT/PCBM layer. As received Sigma PEDOT:PSS could not adhere during spincoating. To achieve film formation, the surface tension of the PEDOT:PSS from Sigma was reduced by adding Zonyl and/or isopropanol. Additionally, the P3HT/PCBM films were treated with UV-ozone to enhance the wetting of the PEDOT:PSS. The received films were difficult to reproduce, sometimes it did not work. However, PEDOT:PSS from Heraeus could be used as received to produce the PEDOT:PSS films on the previously ozone-treated P3HT/PCBM layer.

4.2. Solar Cells

4.2.1. Standard P3HT/PCBM Solar Cells

The averaged initial performances after annealing are listed in Tab.4.2. An example of a P3HT$_{std}$ solar cell is shown in Fig.3.2a.

The first nine samples had low performance due to different reasons. The first two samples had wrong P3HT/PCBM concentrations, then mistakes during annealing were made. Determination of the error source included verification of material quality. Three different P3HT flasks (all already opened) were used and every detail (concentrations, times, looks, etc.) about handling was noted.

sample	$a^2[mm^2]$	$V_{oc}[V]$	I_{sc} $[\mu A]$	$J_{sc}[mA/cm^2]$	P_{mpp} $[\mu W]$	FF[%]	η[%]
P3HT$_{std}$01	5,8	0,54	282	5,0	69	45,7	1,24
P3HT$_{std}$02	4,4	0,53	229	5,3	52	42,8	1,21
P3HT$_{std}$03	5,8	0,58	472	8,2	128	44,7	2,14
P3HT$_{std}$04	3,1	0,59	256	8,3	67	44,3	2,15
P3HT$_{std}$05	4,4	0,58	322	7,3	78	42,4	1,79
P3HT$_{std}$06	4,4	0,57	298	6,9	72	41,0	1,62
P3HT$_{std}$07	5,8	0,61	565	9,7	139	40,5	2,40
P3HT$_{std}$08	4,4	0,59	363	8,3	54	24,9	1,22
P3HT$_{std}$09	4,4	0,62	371	8,5	46	20,2	1,06
P3HT$_{std}$10	3,1	0,61	313	10,1	106	54,9	3,41
P3HT$_{std}$11	3,1	0,61	313	10,1	102	53,4	3,28
P3HT$_{std}$12	3,1	0,62	325	10,5	111	55,3	3,58
P3HT$_{std}$13	3,1	0,61	335	10,8	114	56,2	3,69
P3HT$_{std}$14	4,4	0,61	428	9,9	125	47,5	2,84

Table 4.2.: Initial averaged performances of standard P3HT/PCBM solar cells.

With guided assistance, solar cells P3HT$_{std}$07 - 09 were fabricated. Performances were still insufficient. With a longer cooling time of the P3HT/PCBM blend solution over night and replacement of the syringe filter for every film, from sample P3HT$_{std}$10 on the performances were acceptable. Samples P3HT$_{std}$12-14 were produced with three different P3HTs (material comparison) three days later than samples P3HT$_{std}$10-11. Sample 10 was fabricated with the same blend solution as sample 13. Sample 13 had a slightly higher efficiency ($\eta = 3.69\%$) compared to the similar sample 10 produced three days before ($\eta = 3.41\%$). Sample 11 was produced with the same solution as sample 14. Sample 14 had a visible stain in its center, which could be used as argument for its weaker performance.

One cell (10i) was not usable due to misplaced Al-electrodes. Sample 10i had the same solution as sample 12. With regard to the different P3HT sources, all three flasks delivered more or less similar results. This meant all three P3HTs could be used to produce solar cells. But for better comparison, only one flask was used for the inverted P3HT/PCBM geometry, the one with highest performance used in samples 10 and 13.

The cells were kept in the dark under N_2 atmosphere and measured after 26, 71 and 109 days. The performance of P3HT$_{std}$12 decreased linearly during the ~ 3.5 months from $\eta = 3.58\%$ to $\eta = 3.24\%$, which corresponds to 90% of the initial performance. The V_{oc} remained constant, but J_{sc} decreased slightly from $10.5 mA/cm^2$ to $10.2 mA/cm^2$ and the fill-factor from 55% to 52%. Similar losses were observed for other P3HT$_{std}$ solar cells.

For transient measurements [42][43][44] at ETH Zürich (organic electronics lab in the department of physics), P3HT$_{std}$10 and 14 were encapsulated for transportation. Immediately after encapsulation, the cells had $\sim$ 70% of their previously measured performances. This was attributed to the polymer foil coverage, which was not highly transparent. After three days ($72h$) encapsulated in ambient air, the cell's performances decreased to $\sim$ 85% of the initial performance in encapsulation, which indicated insufficient sealing.

4.2.2. Inverted P3HT/PCBM Solar Cells

The compositions of the solar cells are given in Tab.3.4 and the averaged initial performances in Tab.4.3. For pictures of P3HT$_{inv}$ samples, see Fig.4.9 and Fig.4.10.

The first attempt was unsuccessful, because the PEDOT:PSS (Sigma) did not adhere on the P3HT/PCBM (sample P3HT$_{inv}$01). Longer UV-ozone exposure (up to 1 min) of the P3HT/PCBM lead to better PEDOT:PSS film formation for P3HT$_{inv}$02-04. Samples P3HT$_{inv}$03 and 04 showed short-circuit behaviour. Post fabrication contact treatment (removal of PEDOT:PSS) resulted in damaged solar cells. In [45], a similar device geometry without PEDOT:PSS performed from $\eta = 0.09\%$ to $\eta = 1.5\%$ after 2 h exposure to air. Sample P3HT$_{inv}$02, which had weakest PEDOT:PSS coverage and had initially $\eta = 0.0\%$, showed after exposure to air for 2 min an efficiency $\eta = 0.2\%$. After 30 min, the efficiency decreased again to some $\mu\%$. Therefore, the PEDOT:PSS layer was identified to be the cause for weak solar cells.

This problems were overcome by using "HTL solar" PEDOT:PSS from Heraeus. All following samples were produced with this PEDOT:PSS, which resulted in reproducible film formation (sec.3.4). To avoid short-circuits, PEDOT:PSS was removed from the edges (see e.g. Fig.4.10c).

The next step included investigations about the annealing of the solar cells. P3HT$_{inv}$05 and 06 were pre-annealed before Ag deposition at 130°C for 10 min to dry the PEDOT:PSS. As for the regular geometry [17], pre-annealing resulted in less efficient solar cells. Higher performance was achieved without pre-annealing with P3HT$_{inv}$07, which was annealed for 30 min at 150°C after Ag deposition. The efficiency of sample 05 was enhanced from $\eta = 1.15\%$ to $\eta = 2.1\%$ after eight annealing steps. The solar cell was measured every 15 min after annealing at 150°C (Fig.4.8).

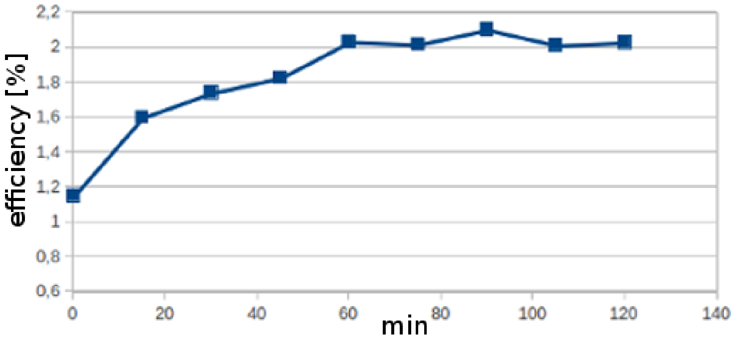

Figure 4.8.: Annealing of P3HT$_{inv}$05

All these solar cells were fabricated on Solaronix TiO_2. The P3HT/PCBM blend formed smooth films on the substrates. For P3HT$_{inv}$09, 11, 13 and 15, sputtered TiO_2 thin films were used. Sample 09 had the amorphous (EB007) type, sample 11 anatase phase (EB008) and samples 13 and 15 the amorphous film with indicated rutile phase (EB009) TiO_2. P3HT/PCBM deposition on sputtered TiO_2 did not result in smooth films, see Fig.4.9. On the rutile containing type, the P3HT/PCBM film coverage was incomplete and the finished solar cells showed no performance (Fig.4.9c). P3HT$_{inv}$09 on the amorphous TiO_2 had no performance as well. On the anatase phase, P3HT/PCBM film formation was inhomogeneous, partly conditioned by the substrate holder during TiO_2 deposition (visible in Fig.4.9b in the right bottom corner). However, averaged performance on anatase was best for the sputtered TiO_2 films with $\eta = 2.27\%$.

For P3HT$_{inv}$ samples 12- 15, the top electrode was evaporated in two steps. After 25 nm

Ag were deposited, the Ag-target was accidentally finished. The solar cells were measured nevertheless but had contact problems. Therefore, another 35 nm Ag were deposited on top. This resulted in the best inverted P3HT/PCBM sample (P3HT$_{inv}$12) with $\eta = 3.13\%$. After this result, the metal electrode thickness was enhanced from 35 nm to 60 nm for all coming solar cells.

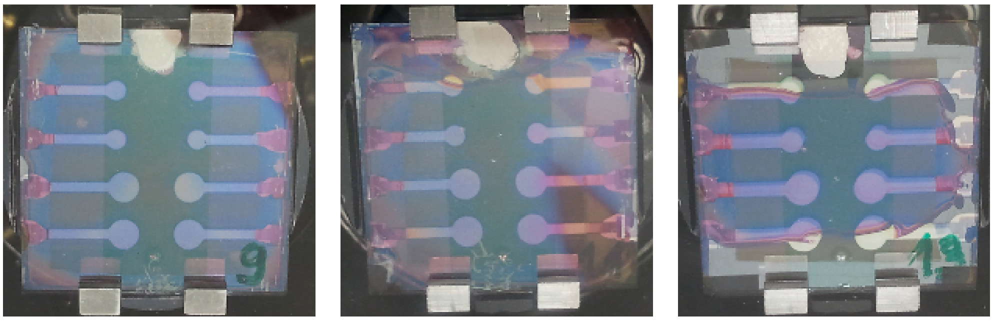

(a) P3HT$_{inv}$09 (b) P3HT$_{inv}$11 (c) P3HT$_{inv}$13

Figure 4.9.: Inverted P3HT/PCBM samples on sputtered TiO_2 substrates. The substrate holders during TiO_2 sputtering are visible in (a) and (b), as there is no TiO_2 deposited. This partly caused inhomogeneous film formation for spin-coated depositions. In (c), weak adhesion of the P3HT/PCBM lead to incomplete film coverage.

The PEDOT:PSS layer was replaced by MoO_3 for samples P3HT$_{inv}$14-18. MoO_3 thickness was varied from 10 nm to 30 nm. Best performance was recorded with 20 nm MoO_3 in P3HT$_{inv}$14 ($\eta = 0.79\%$). The similar produced sample P3HT$_{inv}$17 performed with $\eta = 0.37\%$ not half of P3HT$_{inv}$14. P3HT$_{inv}$17 had higher performance than sample 16 (10 nm MoO_3, $\eta = 0.33\%$) and 18 (30 nm MoO_3, $\eta = 0.22\%$), which were fabricated in the same run as sample 17. See sec.5.2 for the discussion. In Fig.5.1c the IV curve for P3HT$_{inv}$14 cell7 is shown.

The inverted P3HT/PCBM solar cells showed stable behaviour after one to two months stored in the dark under N_2 and performed 3%-10% better as initially (measured for P3HT$_{inv}$08, 10, 12, 19). When exposed to ambient air, the efficiency of P3HT$_{inv}$06 decreased from $\eta = 1.43\%$ within one minute to $\eta = 0.4\%$, followed by a further degradation to zero within one hour.

sample	$a^2[mm^2]$	$V_{oc}[V]$	I_{sc} $[\mu A]$	$J_{sc}[mA/cm^2]$	P_{mpp} $[\mu W]$	FF[%]	$\eta[\%]$
P3HT$_{inv}$02	5,8	0,32	0	0,0	0	0,0	0,00
P3HT$_{inv}$03	4,4	0,34	15	0,3	1	17,7	0,02
P3HT$_{inv}$04	4,4	0,15	4	0,1	0	24,0	0,00
P3HT$_{inv}$05	4,4	0,50	248	5,8	49	39,7	1,15
P3HT$_{inv}$06	3,1	0,51	225	7,3	44	38,5	1,43
P3HT$_{inv}$07	4,4	0,54	368	8,5	94	46,1	2,12
P3HT$_{inv}$08	5,8	0,57	521	9,1	156	52,2	2,70
P3HT$_{inv}$09	3,1	-0,01	0	0,0	0	0,0	0,00
P3HT$_{inv}$10	4,4	0,56	430	9,6	119	49,5	2,67
P3HT$_{inv}$11	4,4	0,58	373	8,7	99	45,1	2,27
P3HT$_{inv}$12	4,4	0,57	455	10,5	136	52,5	3,13
P3HT$_{inv}$13	5,8	0,03	0	0,0	0	57,4	0,00
P3HT$_{inv}$14	5,8	0,39	316	5,4	46	37,2	0,79
P3HT$_{inv}$15	7,1	-0,08	0	0,0	0	0,0	0,00
P3HT$_{inv}$16	4,4	0,31	130	3,0	14	35,5	0,33
P3HT$_{inv}$17	5,8	0,21	149	2,8	20	24,3	0,37
P3HT$_{inv}$18	4,4	0,30	89	2,1	9	34,3	0,22
P3HT$_{inv}$19	4,4	0,55	418	9,6	111	47,6	2,50

Table 4.3.: Initial averaged performances of inverted P3HT/PCBM solar cells. Their composition is given in Table 3.4.

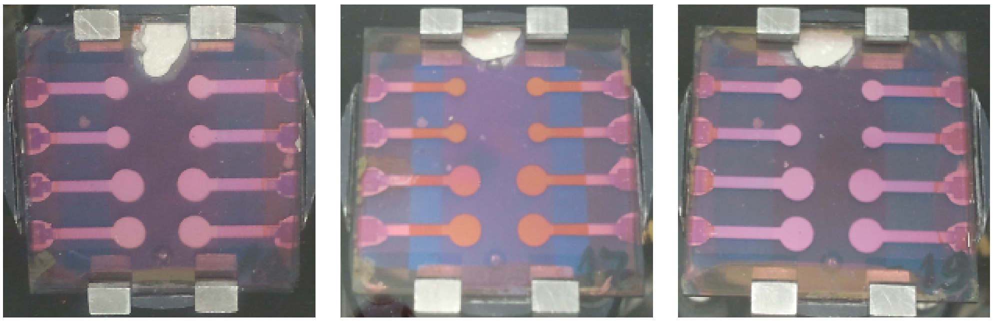

(a) P3HT$_{inv}$12 (b) P3HT$_{inv}$17 (c) P3HT$_{inv}$19

Figure 4.10.: Inverted P3HT/PCBM samples on Solaronix TiO_2 substrates. P3HT$_{inv}$17 had 20 nm MoO_3 deposited instead of PEDOT:PSS. In (a) and (c), the removed PEDOT:PSS on the edges is recognisable.

4.2.3. Inverted Cy-3/C$_{60}$ Solar Cells

The compositions of the layer thicknesses are listed in Tab.3.5 and averaged initial performances in Tab.4.4. Cy-3$_{inv}$ solar cells are shown in Fig.4.11 and Fig.3.3b.

Because of the high surface roughness of the Solaronix TiO_2 (sec.4.1.2, Fig.4.3a), short circuits due to pinholes were feared. Therefore a high C_{60} thickness of 80 nm was chosen for the first four samples on two Solaronix (Cy-3$_{inv}$01, 02) and two sputtered anatase TiO_2 (Cy-3$_{inv}$03, 04) substrates. To find an optimized MoO_3 thickness, 5 nm and 20 nm were compared in the same run. On both TiO_2 substrates, higher efficiencies resulted for 20 nm MoO_3 instead of 5 nm. Solar cells on the sputtered TiO_2 film had higher performance with both 5 and 20 nm MoO_3 than the solar cells on the spin-coated substrate with 20 nm MoO_3 (Cy-3$_{inv}$02). Sample Cy-3$_{inv}$04 (Fig.4.11a) with 20 nm MoO_3 had a promising averaged $\eta = 1.84\%$.

A cross-linkable derivative of PCBM, PCB-diyne, requests the inverted geometry due to deposition order. Next four samples (Cy-3$_{inv}$05-08), using PCB-diyne instead of C_{60}, were produced similarly on two Solaronix and two sputtered anatase TiO_2 substrates with 20 nm MoO_3. Cy-3 films on the PCB-diyne were inhomogenious on the sputtered substrates, but the films on Solaronix substrates were optically of good quality. All samples performed weak with $\eta < 0.1\%$.

To improve Cy-3$_{inv}$04's performance, optimization of the C_{60} thickness was investigated with 40 nm and 60 nm C_{60} instead of 80 nm (Cy-3$_{inv}$09 and 10, see Fig.5.2c). With regard to the efficiency, 60 nm C_{60} was favourable. 40 nm C_{60} delivered in this comparison the weakest performance ($\eta = 1.79\%$), but had the highest averaged FF with 50.2% instead of

$\sim 44\%$. The exciton diffusion length in C_{60} is reported in [46] to be $\sim 40\ nm$. Therefore, $40\ nm\ C_{60}$ was chosen for further investigations.

sample	$a^2[mm^2]$	$V_{oc}[V]$	$I_{sc}\ [\mu A]$	$J_{sc}[mA/cm^2]$	$P_{mpp}\ [\mu W]$	FF[%]	η[%]
Cy-3_{inv}01	5,8	0,28	158	2,8	18	37,0	0,29
Cy-3_{inv}02	7,1	0,50	176	2,5	45	51,8	0,64
Cy-3_{inv}03	5,8	0,74	243	4,3	75	41,3	1,32
Cy-3_{inv}04	7,1	0,85	352	5,0	131	43,3	1,84
Cy-3_{inv}05	4,4	0,44	15	0,3	2	23,1	0,038
Cy-3_{inv}06	4,4	0,21	4	0,1	0	18,1	0,004
Cy-3_{inv}07	4,4	0,08	7	0,2	0	20,2	0,004
Cy-3_{inv}08	4,4	0,07	11	0,2	0	26,4	0,005
Cy-3_{inv}09	5,8	0,84	249	4,3	105	50,2	1,79
Cy-3_{inv}10	4,4	0,86	210	4,8	82	45,4	1,88
Cy-3_{inv}11	4,4	0,86	169	3,9	71	48,8	1,64
Cy-3_{inv}12	4,4	0,86	175	4,1	46	33,8	1,22
Cy-3_{inv}13	4,4	0,84	197	4,5	103	61,7	2,36
Cy-3_{inv}14	4,4	0,67	23	0,8	1	9,9	0,04
Cy-3_{inv}15	5,8	0,89	241	4,3	119	54,7	2,07
Cy-3_{inv}16	3,1	-0,36	0	0,0	0	0,0	0,000
Cy-3_{inv}17	4,4	0,05	182	4,4	1	12,1	0,03
Cy-3_{inv}18	7,1	0,71	191	2,7	25	18,0	0,36
Cy-3_{inv}19	4,4	0,86	145	3,4	41	33,5	0,96
Cy-3_{inv}20	4,4	0,79	162	3,7	76	58,2	1,72
Cy-3_{inv}21	7,1	0,79	199	2,8	41	26,2	0,58

Table 4.4.: Initial averaged performances of inverted Cy-3 solar cells. Their composition is given in Table 3.5.

Inverted Cy-3 solar cells performed better on smooth sputtered TiO_2 than on rough Solaronix substrates. Cy-3_{inv}04, 09 and 10 were deposited on anatase substrates EB008 (with 80% O_2 during deposition) to derive optimal C_{60} thickness. Cy-3_{inv}11-13 were fabricated for a substrate comparison on anatase TiO_2 thin films EB010 (40% O_2 during deposition) and for optimization of the MoO_3 thickness (Fig5.2d). Unfortunately, sample 12 with $20\ nm\ MoO_3$ performed weak with $\eta = 1.22\%$ and was not used for direct substrate comparison. But with Cy-3_{inv}13 (Fig.4.11b), a solar cell with averaged $\eta = 2.36\%$ was produced. The best single solar cell of this sample had $\eta = 2.58\%$ with an FF of 62,99%. After 27 days storage in the glovebox, the cell's performance increased to $\eta = 2.86\%$ (see Fig.5.2b).

Using the same layer thicknesses applied for Cy-3_{inv}13, all sputtered TiO_2 thin films were compared with each other by the next samples Cy-3_{inv}14-17. As listed in Tab.4.4 and shown in Fig.5.2a, only solar cells on anatase phase TiO_2 films resulted in good solar cells. The cells on the amorphous (EB007, Cy-3$_{inv}$14) and rutile containing (EB009 (Cy-3$_{inv}$16), EB011 (Cy-3$_{inv}$17)) films had almost no performance with $\eta < 0.1\%$. Cy-3$_{inv}$15 on EB008 had a performance of $\eta = 2.07\%$, which is 13% weaker than the the similar assembled Cy-3$_{inv}$13 on EB010. The difference between EB008 (80% O_2) and EB010 (40% O_2) is the O_2 content during deposition, but both substrates have anatase phase (Fig.4.2b).

Cy-3$_{inv}$19 (Fig.4.11c) is similarly assembled like Cy-3$_{inv}$15, but a 60 nm gold electrode was evaporated instead of silver. Cy-3$_{inv}$19 performed weak with $\eta = 0.96\%$ compared to $\eta = 2.07\%$ of Cy-3$_{inv}$15. Also sample 21 with a gold electrode performed below 1%. With Cy-3$_{inv}$18-21, experiments in order to try doping for better performances were attempted. In [47] an enhanced performance of cyanine bilayer solar cells is reported, when the cells were exposed to oxygen. The Cy-3 layers of samples 18, 20 and 21 were exposed for 10s to UV-ozone, which should induce a p-doping. Cy-3$_{inv}$18 was on anatase EB008, but performed weak after oxygen-doping with $\eta = 0.36\%$. Similar p-doped Cy-3 from sample Cy-3$_{inv}$20 was deposited on a EB008 substrate, which was exposed for 10h to x-rays during GIXRD measurement. This could have induced a n-doping of the TiO_2, Cy-3$_{inv}$20 reached even after the harming ozone treatment $\eta = 1.72\%$.

Regarding stability, all followed samples (Cy-3$_{inv}$04, 13, 15 and 20) increased their performances after several days by $\sim$ 10%. No degradation was recognised, even after exposure for 6 h to ambient air under illumination.

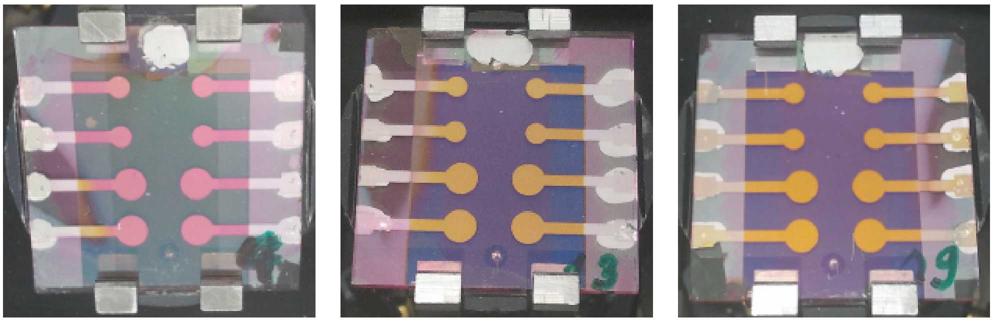

(a) Cy-3$_{inv}$04 (b) Cy-3$_{inv}$13 (c) Cy-3$_{inv}$19

Figure 4.11.: Inverted Cy-3 solar cells

5. Discussion

5.1. Titanium Dioxide

One goal was to fabricate several Ti-oxide thin films and their comparison. Using reactive RF magnetron sputtering, different TiO_2 thin films were obtained by changing sputtering conditions. Deposited TiO_2 films with anatase or rutile phase were acquired on ITO, which served as a seed layer for the crystals (Fig.4.2a). On amorphous glass, with the same sputtering conditions less crystalline films were deposited. The substrate has a strong influence on the film, also e.g. in [27] the similar sol-gel route resulted in different TiO_2 for depositions on ITO and FTO. In publications about RF sputtered TiO_2 (sec.2.2), usually films of several hundred nm deposited on highly crystalline substrates are discussed. Here, crystalline phases were obtained already for films of $\sim 40\ nm$.

A recipe for a spin-coated anatse TiO_2 film was worked out. These films were rough (RMS surface roughness of $11.5nm$) compared to sputtered films, which could be attributed on agglomerations of the TiO_2 nanoparticles. The obtained sputtered anatase TiO_2 films were smooth with RMS roughness $< 1\ nm$. Sputtered rutile containing films EB009 and EB011 formed spikes on their surface, which lead to higher RMS roughnesses of $2.7\ nm$ and $7.3\ nm$. The high roughness for the DC sputtered EB011 can also be explained with its fast deposition rate of $1.5Å/s$ compared to the RF sputtered films with a slow deposition rate of $\sim 0.04Å/s$. The slow deposition rate is partly caused by high O_2 partial pressures, which limits the Ar content and hence the plasma power during sputtering. In general, DC sputtering is considerably faster.

Rutile films were more hydrophilic than anatase and amorphous films. The rather hydrophobic P3HT/PCBM solution did only partly adhere on rutile containing TiO_2 (Fig.4.9c). This could be caused by the spikes on the surface (Fig.4.4a), which provoked de-wetting in analogy of an inverted lotus effect.

5.2. P3HT/PCBM Bulk Heterojunction Solar Cells

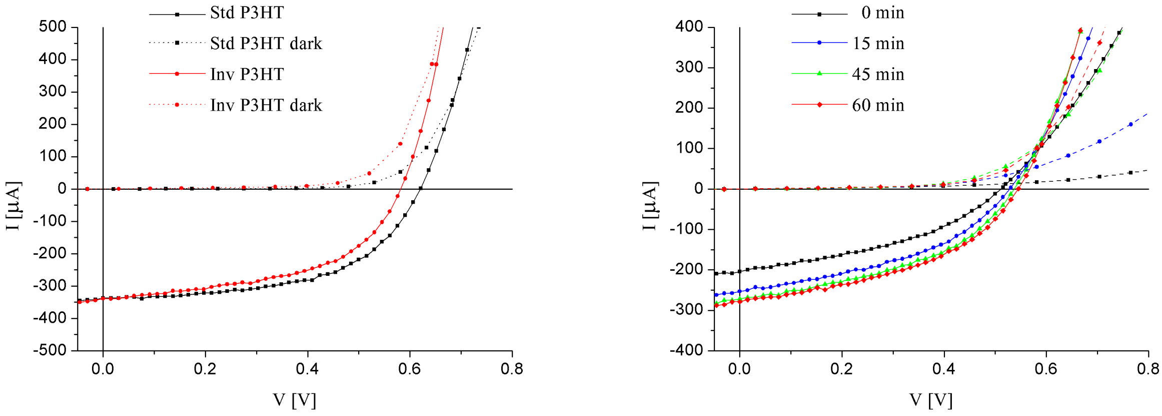

(a) Standard and inverted P3HT/PCBM geometry in direct comparison

(b) Effect of annealing for the inverted geometry

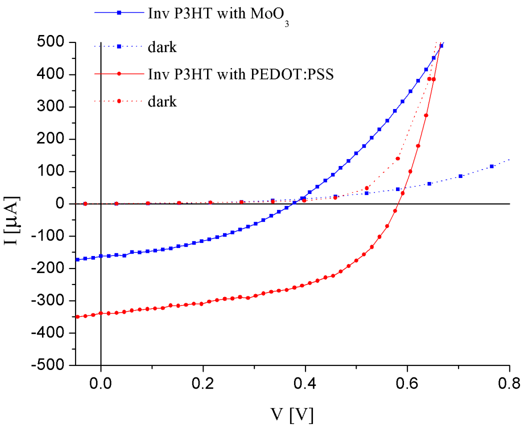

(c) Inverted geometry with PEDOT:PSS or MoO_3 as hole collecting layer

Figure 5.1.: IV characteristics of P3HT/PCBM solar cells

Fig.5.1 summarizes IV characteristics of P3HT/PCBM solar cells. Fig.5.1a shows the direct comparison of the best performing standard (P3HT$_{std}$13 cell2) and best performing inverted (P3HT$_{inv}$12 cell1) solar cell. The standard configuration had $V_{oc} = 0.61\ V$, $J_{sc} = 11.0\ mA/cm^2$, $FF = 55.7\%$ resulting in an efficiency of $\eta = 3.73\%$. The inverted configuration reached $V_{oc} = 0.56\ V$, $J_{sc} = 11.0\ mA/cm^2$, $FF = 52.2\%$ which gives an efficiency of $\eta = 3.27\%$. Compared to reported values ($\eta \simeq 5\%$ [17]), the here presented regular geometry is not outstanding. But the focus was not on the improvement of standard P3HT/PCBM solar cells, these solar cells were produced to learn and improve the fabrication skills. Its inverted structure reached almost similar values, which is astonishing since best reported values for related inverted P3HT/PCBM structures (differing in the top metal electrode: gold instead of silver) are with $\eta = 3.81\%$ [48] not significantly higher. The here presented record cell P3HT$_{inv}$12 cell1 outperforms several reported (amongst others "highly efficient") inverted P3HT/PCBM based cells, e.g. [24] [25] [26] [28]. For a critical discussion it has to be mentioned, that the best solar cell P3HT$_{inv}$12 was reproduced (P3HT$_{inv}$19), but it resulted in weaker efficiency. The best performing solar cell of P3HT$_{inv}$19 cell7 delivered $V_{oc} = 0.56\ V$, $J_{sc} = 10.9\ mA/cm^2$, $FF = 49.0\%$ and $\eta = 3.01\%$, which is 92% of the efficiency of P3HT$_{inv}$12 cell1. This could be explained by different P3HT/PCBM blend solutions or slightly different PEDOT:PSS films (see sec.4.1.6). Reproducibility is difficult to obtain for these solar cells.

In Fig.5.1b the annealing effect (Fig.4.8) is drawn in terms of IV characteristics. P3HT$_{inv}$05 cell7 initially delivered $V_{oc} = 0.51\ V$, $J_{sc} = 6.5\ mA/cm^2$, $FF = 40.2\%$ resulting in an efficiency of $\eta = 1.33\%$. After four annealing steps, its performance increased to $V_{oc} = 0.54\ V$, $J_{sc} = 9.0\ mA/cm^2$, $FF = 44.3\%$ with an efficiency of $\eta = 2.13\%$. Annealing mainly increased the charge carrier mobility in the BHJ, which lead to higher short-circuit currents.

In [49], an inverted P3HT/PCBM solar cell with MoO_3 as hole collecting layer is reported to reach $\eta = 3.86\%$. Replacing the PEDOT:PSS layer by MoO_3 decreased the power, as shown in Fig.5.1c. Drawn is again P3HT$_{inv}$12 cell1 as best inverted P3HT/PCBM compared to the best performing solar cell with MoO_3 (P3HT$_{inv}$14 cell7) with $V_{oc} = 0.37\ V$, $J_{sc} = 5.3\ mA/cm^2$, $FF = 38.6\%$ resulting in a poor efficiency of $\eta = 0.76\%$.

The conductivity of PEDOT:PSS depends on several factors like film thickness, PEDOT to PSS proportion or storage solvent. For this work, several PEDOT:PSSs were used (sec.3.3). PEDOT:PSS from Sigma was used for standard geometry and is pure H_2O based, but in the PEDOT:PSS from Heraeus, used for the inverted geometry, other solvents were included, which enhanced the wetting on P3HT/PCBM films. Unfortunately no informations about these additional solvents/chemicals are given, but with a certain probability the added materials are related to the tested Zonyl and isopropanol for the Sigma PEDOT:PSS (see sec.4.2.2). In [50], Zonyl and dimethylsulfoxide (DMSO) are added to PEDOT:PSS to enhance its conductivity on flexible substrates. In sec.4.1.6 it was derived, that reproducibility of exactly similar PEDOT:PSS films is difficult to maintain.

With regard to the UV-Vis absorption (Fig.4.7c), the inverted architecture absorbs less than the standard from $\lambda = 800 - 600\ nm$. This may originate from interference effects on the different substrates. After annealing, the absorption of the blend increased for both cases to ~ 0.5 at $\lambda = 500\ nm$, which is in good agreement for efficient solar cells regarding the copied recipe [17]. This is confirming the height measurements of the P3HT/PCBM films with the profilometer, which gave for both cases a height of $\sim 100\ nm$.

The inverted P3HT/PCBM solar cells performed better on the rough Solaronix TiO_2 than on the sputtered TiO_2 anatase thin film. On sputtered amorphous and rutile TiO_2 thin films, no performance was measured. Adhesion of the P3HT/PCBM blend was higher on the spin-coated TiO_2 film than on sputtered TiO_2. The hydrophobic P3HT/PCBM blend solution had better adhesion on a rough hydrophilic surface than on a smooth one, since the centripetal force during spin-coating drives the solution off the substrates. On a rough TiO_2 surface, the interface of the BHJ with the n-type TiO_2 is enhanced and hence could lead to better performances. The height of the P3HT/PCBM film is with $\sim 100\ nm$ not highly critical and was obtained for both regular and inverted geometry with the same experimental procedures.

5.3. Inverted Cy-3/C_{60} Bilayer Heterojunction Solar Cells

The bilayer heterojunction between Cy-3 and C_{60} theoretically requires a smooth, planar surface (Fig.2.3a). Therefore the sputtered TiO_2 films were ideal candidates as substrates. By the first experiment with Cy-3 solar cells, samples on rough Solaronix substrates showed much weaker performances than solar cells on smooth sputtered anatase TiO_2.

In Fig.5.2a, a TiO_2 substrate comparison is shown for the Cy-3_{inv} assebly ITO(150 nm)/ TiO_2($\sim 40\ nm$)/ C_{60}(40 nm)/ Cy-3(16 nm)/ MoO_3(30 nm)/ Ag(60 nm). The best achieved Cy-3_{inv} solar cells were assembled in this configuration, which had a total thickness of $\sim$ 336 nm. Therefore these solar cells belong to the category of thin film solar cells. Reasonable performances resulted only on anatase phase TiO_2, which were substrates EB008 and EB010. It can be seen, that the FF for EB010 (green curve) is higher than the FF for EB008 (red). The solar cells on the amorphous substrates EB007 and EB009 (EB009 contained also small rutile phase) showed no photo-induced I_{sc}, whereas the rutile EB011 had short-circuit behaviour attributed to the high spikes on the TiO_2 surface (Fig4.4c). Shown are the best small (3.1 mm^2) solar cells of Cy-3_{inv}13 and Cy-3_{inv}15 when they were measured immediately after fabrication. Data was:
Cy-3_{inv}13 cell2 (EB010): $V_{oc} = 0.84\ V$, $J_{sc} = 4.9\ mA/cm^2$, $FF = 63.0\%$, $\eta = 2.58\%$
Cy-3_{inv}15 cell2 (EB008): $V_{oc} = 0.89\ V$, $J_{sc} = 4.7\ mA/cm^2$, $FF = 51.0\%$, $\eta = 2.15\%$.

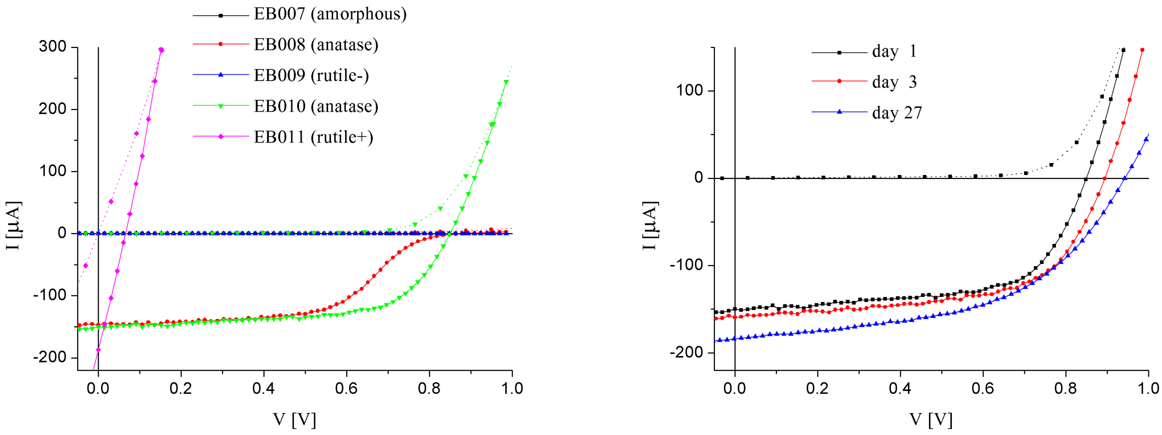

(a) Substrate comparison

(b) Time evolution of Cy-3_{inv}13

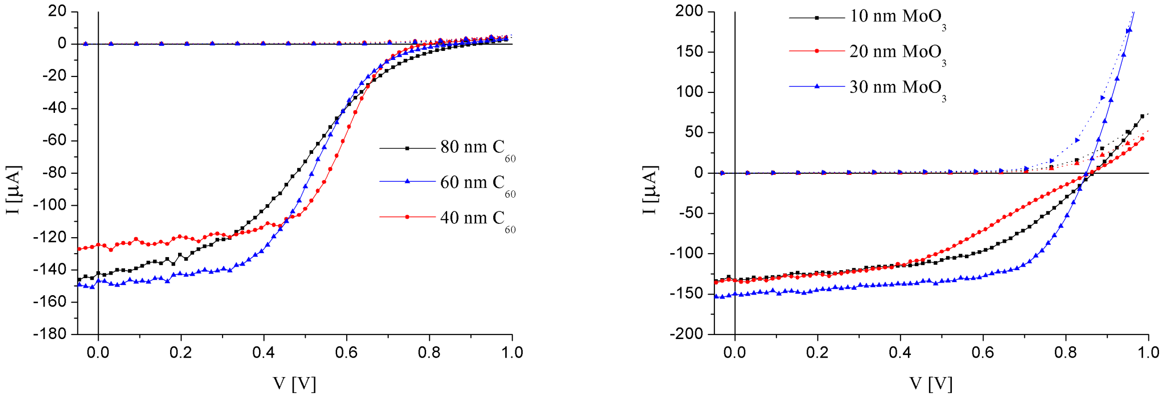

(c) Study on C_{60} thickness

(d) Study on MoO_3 thickness

Figure 5.2.: IV characteristics of inverted Cy-3 solar cells

The tendency, that solar cells on EB010 had higher FF than cells on EB008 can also be recognised by comparison of IV data with solar cells deposited on EB008 (Fig.5.2c) and solar cells deposited on EB010 (Fig.5.2d). The higher O_2 content during deposition for EB008 could have induced a slightly over-oxidized TiO_2. This might enhanced the resistivity for electrons to enter the TiO_2 of EB008, which resulted in lower FF.

In Fig.5.2b the IV curves of the mentioned best Cy-3_{inv}13 cell2 are shown after 1, 3 and 27 days. Initially it had $\eta = 2.58\%$, but after 27 days storage in the dark under N_2 in the glove-box it performed with an efficiency of $\eta = 2.86\%$. Exact data was:
after day 1: $V_{oc} = 0.84\ V$, $J_{sc} = 4.9\ mA/cm^2$, $FF = 63.0\%$, $\eta = 2.58\%$
after day 27:$V_{oc} = 0.94\ V$, $J_{sc} = 5.9\ mA/cm^2$, $FF = 51.4\%$, $\eta = 2.86\%$.

The initially high FF decreased, but the already high V_{oc} and the I_{sc} increased, which resulted in a $\sim$ 10% better performance of this cell after 27 days. In [51] the highest performance of a cyanine based bilayer solar cell is reported with $V_{oc} = 0.72\ V$, $J_{sc} = 6.9\ mA/cm^2$, $FF = 61\%$ and $\eta = 3.0\%$. The here presented solar cell is close to this record cell concerning η. If the transmittance loss of $\sim$ 9%, which is caused by the sample holder cover glass, is taken into account, Cy-3$_{inv}$13 cell2 has an expected efficiency of 3.14%.

In Fig.5.2c the optimization regarding the C$_{60}$ thickness is shown. The solar cells were deposited on EB008 TiO_2 and had a MoO_3 thickness of 20 nm. Shown are small (3.1 mm^2) solar cells of the corresponding samples. Data was:
Cy-3$_{inv}$04 cell2 (80 nm C$_{60}$): $V_{oc} = 0.91\ V$, $J_{sc} = 4.6\ mA/cm^2$, $FF = 31.4\%$, $\eta = 1.32\%$
Cy-3$_{inv}$10 cell8 (60 nm C$_{60}$): $V_{oc} = 0.86\ V$, $J_{sc} = 4.8\ mA/cm^2$, $FF = 39.4\%$, $\eta = 1.64\%$
Cy-3$_{inv}$09 cell2 (40 nm C$_{60}$): $V_{oc} = 0.82\ V$, $J_{sc} = 4.0\ mA/cm^2$, $FF = 49.8\%$, $\eta = 1.65\%$

With regard to FF, the most promising C$_{60}$ thickness was 40 nm. In literature 40 nm are reported to be the exciton diffusion lenght in C$_{60}$ [46]. Even though I_{sc} was slightly reduced due to thinner C$_{60}$, the thickness of 40 nm was chosen as optimized thickness.

In Fig.5.2d the different thicknesses of MoO_3 on EB010 of samples Cy-3$_{inv}$11-13 are shown. Again data for initially best small (3.1 mm^2) solar cells are plotted. With Cy-3$_{inv}$13 cell2, the best achieved cell is listed here again. Data was:
Cy-3$_{inv}$11 cell8 (10 nm MoO_3): $V_{oc} = 0.86\ V$, $J_{sc} = 4.3\ mA/cm^2$, $FF = 51.0\%$, $\eta = 1.87\%$
Cy-3$_{inv}$12 cell8 (20 nm MoO_3): $V_{oc} = 0.86\ V$, $J_{sc} = 4.3\ mA/cm^2$, $FF = 42.8\%$, $\eta = 1.58\%$
Cy-3$_{inv}$13 cell2 (30 nm MoO_3): $V_{oc} = 0.84\ V$, $J_{sc} = 4.9\ mA/cm^2$, $FF = 63.0\%$, $\eta = 2.58\%$

Obviously, 30 nm MoO_3 resulted in the best performance.

Experiments with Cy-3$_{inv}$ solar cells in ambient air under illumination were performed by Dr. G. Wicht. He measured no degradation of the solar cell even after 6 h, which is very promising with regard to its stability. PhD student Hui Zhang confirmed earlier, that his in standard geometry assembled bilayer solar cells degraded much slower in ambient air, when he evaporated a 40 nm MoO_3 encapsulation layer over the finished solar cells. Therefore the stability may be attributed to the shielding of the MoO_3 layer.

The increase in performance of $\sim$ 10% for Cy-3$_{inv}$04, 13, 15 and 20 was an astonishing observation and no simple explanation was found. It might be originated by the counterion diffusion in the Cy-3 layer towards the MoO_3 and hence changed interface properties enhanced the V_{oc} on cost of the FF. Longer surveillance of the corresponding samples would be interesting in any case, as well as biasing the cells to investigate the solar cells reaction in terms of performance.

5.4. Outlook

With the presented results, further optimizations for inverted Cy-3_{inv} solar cells are possible and a new record cell seems in reaching distance. Higher FF was shown for solar cells deposited on sputtered anatase with lower O_2 content in the deposition plasma. Hence a deposition of anatase TiO_2 under a further decreased O_2 content could enhance the performance. It might be that the TiO_2 anatase film deposited with 80% O_2 in the plasma was slightly over-oxidized, resulting in smaller electron mobility in the thin film. Rutherford backscattering spectrometry (RBS) could help to determine the exact oxygen content of the TiO_{2+x} film, but since the deposited films are very thin it is not certain whether this measurement would be successful.

Further TiO_2 surface modifications could be investigated. Reducing the surface by a diluted base or annealing under an applied hydrogen flow could induce a n-doping. Also a amphiphilic layer in between the TiO_2 and the C_{60} could help to enhance charge carrier transport, described e.g. in [52].

On the other hand, thickness optimizations could be continued. The reported cyanine based record solar cell [51] had a cyanine layer thickness of 30 nm. In this study $\sim$ 16 nm cyanine were used, since this was the used Cy-3 film thickness for the first samples and it remained unchanged for comparison. The C_{60} thickness could be further reduced as well as the MoO_3 layer could be increased, since for both layers edge values were taken as optimized layer thickness.

First experiments of the solar cell in ambient air indicated already good stability. Further studies hopefully verify highly stable, more efficient inverted cyanine bilayer heterojunction solar cells.

Nevertheless, some control experiments would help to confirm the presented values. It was remarked, that reproducibility is difficult to obtain. The record assembly of ITO(150 nm)/ TiO_2($\sim$ 40 nm)/ C_{60}(40 nm)/ Cy-3(16 nm)/ MoO_3(30 nm)/ Ag(60 nm) should be deposited on a Solaronix TiO_2 substrate to clearly identify that sputtered TiO_2 thin films are requested. Also an AFM scan of the C_{60} layer on the TiO_2 would be useful to better understand the cell's morphology.

6. Closing Words

I would like to thank to many people, who made this work possible.

First, I thank Prof. Ernst Meyer for accepting this thesis for the nanoscience curriculum at University of Basel. Without the authentication, this work was not possible. Then I would like to thank Dr. Roland Hany, who initiated this thesis on demand and offered me a working place at EMPA Dübendorf. Without his valuable inputs, ideas and hints, this work would not have been so successful. I would like to thank Dr. Geatan Wicht and Hui Zhang for introducing me into solar cell fabrication. I thank Timo Jäger of the photovoltaics and thin films lab at EMPA for the assistance and fabrication of sputtered TiO_2 thin films. Then, I thank Jean-Nicolas Tisserand for general help throughout this work. Of course, the whole group of Prof. Alain Nüesch has deserved my special thanks for friendly support and inspiring talks. Also I thank Dr. Songhak Yoon and Dr. Erik Lewin at EMPA for introducing me into GIXRD measurements. I thank Dr. Fabio la Mattina for helpful suggestions concerning 4-wire measurements. Last but not least I would like to thank my parents, my sisters and my most charming girlfriend for their unconditional love and support.

Bibliography

[1] *Schweizerische Gesamtenergiestatistik 2011.* Bundesamt für Energie, Bern (Switzerland), 2011. www.bundespublikationen.admin.ch.

[2] *Energieverbrauch in Deutschland.* Bundesministerium für Umwelt, Naturschutz und Reaktorsicherheit, Berlin (Germany), 2011.

[3] A. Einstein, “ Über einen die Erzeugung und Verwandlung des Lichtes betreffenden heuristischen Gesichtspunkt,” *Annalen der Physik*, vol. 17, no. 6, pp. 132–148, 1905.

[4] D. M. Chapin, C. S. Fuller, and G. L. Pearson, “A new silicon p-n junction photocell for converting solar radiation into electrical power,” *Journal of Applied Physics*, vol. 25, no. 5, pp. 676–677, 1954.

[5] M. A. Green, K. Emery, Y. Hishikawa, and W. Warta, “Solar cell efficiency tables (version 37),” *Progress in Photovoltaics: Research and Applications*, vol. 19, no. 1, pp. 84–92, 2011.

[6] P. Würfel, *Physik der Solarzellen.* Heidelberg, Berlin (Germany): Spektrum Akademischer Verlag, 2000.

[7] M. A. Green, *Third Generation Photovoltaics : Advanced Solar Energy Conversion.* Heidelberg, Berlin (Germany): Springer, 2006.

[8] J. Nelson, *The Physics of Solar Cells.* London (England): Imperial College Press, 2003.

[9] Hoppe, H. and Sariciftci, N.S., “Organic solar cells: An overview,” *J. Mater. Res.*, vol. 19, pp. 1924–1945, JUL 2004.

[10] C. W. Tang, “Two-layer organic photovoltaic cell,” *Applied Physics Letters*, vol. 48, no. 2, pp. 183–185, 1986.

[11] P. Peumans, S. Uchida, and S. R. Forrest, "Efficient bulk heterojunction photovoltaic cells using small-molecular-weight organic thin films," *Nature*, vol. 425, pp. 158–162, 2003.

[12] B. O'Regan and M. Grätzel, "A low-cost, high-efficiency solar cell based on dye-sensitized colloidal titanium dioxide films," *Nature*, vol. 353, pp. 737–740, 1991.

[13] G. Yu, C. Zhang, K. Pakbaz, and A. Heeger, "Photonic devices made with semiconducting conjugated polymers: New developments," *Synthetic Metals*, vol. 71, no. 1–3, pp. 2241 – 2242, 1995.

[14] T. A. Chen and R. D. Rieke, "The first regioregular head-to-tail poly(3-hexylthiophene-2,5-diyl) and a regiorandom isopolymer: nickel versus palladium catalysis of 2(5)-bromo-5(2)-(bromozincio)-3-hexylthiophene polymerization," *Journal of the American Chemical Society*, vol. 114, no. 25, pp. 10087–10088, 1992.

[15] H. Sirringhaus, P. J. Brown, R. H. Friend, M. M. Nielsen, K. Bechgaard, B. M. W. Langeveld-Voss, A. J. H. Spiering, R. A. J. Janssen, E. W. Meijer, P. Herwig, and D. M. de Leeuw, "Two-dimensional charge transport in self-organized, high-mobility conjugated polymers," *Nature*, vol. 401, pp. 685–688, 1999.

[16] F. Padinger, R. Rittberger, and N. Sariciftci, "Effects of postproduction treatment on plastic solar cells," *Advanced Functional Materials*, vol. 13, no. 1, pp. 85–88, 2003.

[17] W. Ma, C. Yang, X. Gong, K. Lee, and A. Heeger, "Thermally stable, efficient polymer solar cells with nanoscale control of the interpenetrating network morphology," *Advanced Functional Materials*, vol. 15, no. 10, pp. 1617–1622, 2005.

[18] S.-S. Sun and N. S. Sariciftci, *Organic Photovoltaics: Mechanisms, Materials and Devices.* Boca Raton (USA): Taylor and Francis Group, 2005.

[19] M. Grätzel and J. R. Durrant, *Nanostructured And Photoelectrochemical Systems For Solar Photon Conversion, chapter 8: Dye-Sensitised Mesoscopic Solar Cells.* London (England): Imperial College Press, 2005.

[20] V. D. Edited by Christoph Brabec and U. Scherf, *Organic Photovoltaics.* Weinheim (Germany): Wiley-VCH, 2008.

[21] M. D. Earle, "The electrical conductivity of titanium dioxide," *Phys. Rev.*, vol. 61, pp. 56–62, Jan 1942.

[22] U. Diebold, “The surface science of titanium dioxide,” *Surface Science Reports*, vol. 48, no. 5–8, pp. 53 – 229, 2003.

[23] A. Fujishima, X. Zhang, and D. A. Tryk, “Titanium dioxide photocatalysis and related surface phenomena,” *Surface Science Reports*, vol. 63, no. 12, pp. 515 – 582, 2008.

[24] T. Kuwabara, T. Nakayama, K. Uozumi, T. Yamaguchi, and K. Takahashi, “Highly durable inverted-type organic solar cell using amorphous titanium oxide as electron collection electrode inserted between indium tin oxide and organic layer,” *Solar Energy Materials and Solar Cells*, vol. 92, no. 11, pp. 1476 – 1482, 2008.

[25] C. Waldauf, M. Morana, P. Denk, P. Schilinsky, K. Coakley, S. A. Choulis, and C. J. Brabec, “Highly efficient inverted organic photovoltaics using solution based titanium oxide as electron selective contact,” *Applied Physics Letters*, vol. 89, no. 23, p. 233517, 2006.

[26] M. M. Voigt, R. C. Mackenzie, C. P. Yau, P. Atienzar, J. Dane, P. E. Keivanidis, D. D. Bradley, and J. Nelson, “Gravure printing for three subsequent solar cell layers of inverted structures on flexible substrates,” *Solar Energy Materials and Solar Cells*, vol. 95, no. 2, pp. 731 – 734, 2011.

[27] M. Lira-Cantu, A. Chafiq, J. Faissat, I. Gonzalez-Valls, and Y. Yu, “Oxide/polymer interfaces for hybrid and organic solar cells: Anatase vs. rutile titanium dioxide,” *Solar Energy Materials and Solar Cells*, vol. 95, no. 5, pp. 1362 – 1374, 2011.

[28] H. Oh, J. Krantz, I. Litzov, T. Stubhan, L. Pinna, and C. J. Brabec, “Comparison of various sol–gel derived metal oxide layers for inverted organic solar cells,” *Solar Energy Materials and Solar Cells*, vol. 95, no. 8, pp. 2194 – 2199, 2011.

[29] C.-Y. Li, T.-C. Wen, T.-H. Lee, T.-F. Guo, J.-C.-A. Huang, Y.-C. Lin, and Y.-J. Hsu, “An inverted polymer photovoltaic cell with increased air stability obtained by employing novel hole/electron collecting layers,” *J. Mater. Chem.*, vol. 19, pp. 1643–1647, 2009.

[30] N. Martin, C. Rousselot, D. Rondot, F. Palmino, and R. Mercier, “Microstructure modification of amorphous titanium oxide thin films during annealing treatment,” *Thin Solid Films*, vol. 300, no. 1–2, pp. 113 – 121, 1997.

[31] P. Zeman and S. Takabayashi, “Self-cleaning and antifogging effects of titaniumdioxide films prepared by radio frequency magnetron sputtering,” *Journal of Vacuum Science and Technology A: Vacuum, Surfaces, and Films*, vol. 20, no. 2, pp. 388–393, 2002.

[32] Z. P. and T. S., “Effect of total and oxygen partial pressures on structure of photocatalytic titaniumdioxide films sputtered on unheated substrate,” *Surface and Coatings Technology*, vol. 153, no. 1, pp. 93–99, 2002.

[33] K. Okimura, “Low temperature growth of rutile titanium dioxide films in modified rf magnetron sputtering,” *Surface and Coatings Technology*, vol. 135, no. 2–3, pp. 286 – 290, 2001.

[34] C. Sarra-Bournet, C. Charles, and R. Boswell, “Low temperature growth of nanocrystalline titanium dioxide films with argon/oxygen low-field helicon plasma,” *Surface and Coatings Technology*, vol. 205, no. 15, pp. 3939 – 3946, 2011.

[35] B.-S. Jeong, D. Norton, and J. Budai, “Conductivity in transparent anatase titanium dioxide films epitaxially grown by reactive sputtering deposition,” *Solid-State Electronics*, vol. 47, no. 12, pp. 2275 – 2278, 2003.

[36] P. Song, Y. Irie, and Y. Shigesato, “Crystallinity and photocatalytic activity of titanium dioxide films deposited by reactive sputtering with radio frequency substrate bias,” *Thin Solid Films*, vol. 496, no. 1, pp. 121 – 125, 2006.

[37] S. Mraz and J. M. Schneider, “Structure evolution of magnetron sputtered titanium dioxide thin films,” *Journal of Applied Physics*, vol. 109, no. 2, p. 023512, 2011.

[38] D.-S. Leem, A. Edwards, M. Faist, J. Nelson, D. D. C. Bradley, and J. C. de Mello, “Efficient organic solar cells with solution-processed silver nanowire electrodes,” *Advanced Materials*, vol. 23, no. 38, pp. 4371–4375, 2011.

[39] O. Malinkiewicz, M. Lenes, H. Brine, and H. J. Bolink, “Meniscus coated high open-circuit voltage bi-layer solar cells,” *RSC Adv.*, vol. 2, pp. 3335–3339, 2012.

[40] D. E. Vaughan, “Four-probe resistivity measurements on small circular specimens,” *British Journal of Applied Physics*, vol. 12, no. 8, p. 414, 1961.

[41] *RM3-AR Instructions.* Jandel Engineering Limited (UK), 2012. Useful equations.

[42] C. R. McNeill, I. Hwang, and N. C. Greenham, “Photocurrent transients in all-polymer solar cells: Trapping and detrapping effects,” *Journal of Applied Physics*, vol. 106, no. 2, p. 024507, 2009.

[43] I. Hwang, C. R. McNeill, and N. C. Greenham, “Drift-diffusion modeling of photocurrent transients in bulk heterojunction solar cells,” *Journal of Applied Physics*, vol. 106, no. 9, p. 094506, 2009.

[44] Z. Li, F. Gao, N. C. Greenham, and C. R. McNeill, “Comparison of the operation of polymer/fullerene, polymer/polymer, and polymer/nanocrystal solar cells: A transient photocurrent and photovoltage study,” *Advanced Functional Materials*, vol. 21, no. 8, pp. 1419–1431, 2011.

[45] C. S. Kim, S. S. Lee, E. D. Gomez, J. B. Kim, and Y.-L. Loo, “Transient photovoltaic behavior of air-stable, inverted organic solar cells with solution-processed electron transport layer,” *Applied Physics Letters*, vol. 94, no. 11, p. 113302, 2009.

[46] P. Peumans, A. Yakimov, and S. R. Forrest, “Small molecular weight organic thin-film photodetectors and solar cells,” *Journal of Applied Physics*, vol. 93, no. 7, pp. 3693–3723, 2003.

[47] B. Fan, R. Hany, J.-E. Moser, and F. Nüesch, “Enhanced cyanine solar cell performance upon oxygen doping,” *Organic Electronics*, vol. 9, no. 1, pp. 85 – 94, 2008.

[48] T. Kuwabara, H. Sugiyama, M. Kuzuba, T. Yamaguchi, and K. Takahashi, “Inverted bulk-heterojunction organic solar cell using chemical bath deposited titanium oxide as electron collection layer,” *Organic Electronics*, vol. 11, no. 6, pp. 1136 – 1140, 2010.

[49] D. Zhao, S. Tan, L. Ke, P. Liu, A. Kyaw, X. Sun, G. Lo, and D. Kwong, “Optimization of an inverted organic solar cell,” *Solar Energy Materials and Solar Cells*, vol. 94, no. 6, pp. 985 – 991, 2010.

[50] M. Vosgueritchian, D. J. Lipomi, and Z. Bao, “Highly conductive and transparent pedot:pss films with a fluorosurfactant for stretchable and flexible transparent electrodes,” *Advanced Functional Materials*, vol. 22, no. 2, pp. 421–428, 2012.

[51] B. Fan, F. Araujo de Castro, B. T.-T. Chu, J. Heier, D. Opris, R. Hany, and F. Nuesch, “Improved performance of cyanine solar cells with polyaniline anodes,” *J. Mater. Chem.*, vol. 20, pp. 2952–2955, 2010.

[52] Y.-C. Huang, W.-C. Yen, Y.-C. Liao, Y.-C. Yu, C.-C. Hsu, M.-L. Ho, P.-T. Chou, and W.-F. Su, “Band gap aligned conducting interface modifier enhances the performance of thermal stable polymer-titanium dioxide nanorod solar cell,” *Applied Physics Letters*, vol. 96, no. 12, p. 123501, 2010.

A. Declaration of Scientific Fidelity

AIP | Applied Physics Letters

Influence of crystalline titanium oxide layer smoothness on the performance of inverted organic bilayer solar cells

Etienne Berner, Timo Jäger, Thomas Lanz, Frank Nüesch, Jean-Nicolas Tisserant et al.

Citation: Appl. Phys. Lett. **102**, 183903 (2013); doi: 10.1063/1.4804599

View online: http://dx.doi.org/10.1063/1.4804599

View Table of Contents: http://apl.aip.org/resource/1/APPLAB/v102/i18

Published by the American Institute of Physics.

APPLIED PHYSICS LETTERS **102**, 183903 (2013)

Influence of crystalline titanium oxide layer smoothness on the performance of inverted organic bilayer solar cells

Etienne Berner,[1,a)] Timo Jäger,[2,a)] Thomas Lanz,[3] Frank Nüesch,[1,4]
Jean-Nicolas Tisserant,[1] Gaetan Wicht,[1] Hui Zhang,[1] and Roland Hany[1,b)]
[1]*Empa, Swiss Federal Institute for Materials Science and Technology, Laboratory for Functional Polymers, CH-8600 Dübendorf, Switzerland*
[2]*Empa, Swiss Federal Institute for Materials Science and Technology, Laboratory for Thin Films and Photovoltaics, CH-8600 Dübendorf, Switzerland*
[3]*Institute of Computational Physics, ZHAW, Zürich University of Applied Sciences, CH-8401 Winterthur, Switzerland*
[4]*Institut des Matériaux, Ecole Polytechnique Fédéral de Lausanne, EPFL Station 12, CH-1015 Lausanne, Switzerland*

(Received 6 March 2013; accepted 21 April 2013; published online 10 May 2013)

Due to the small exciton diffusion length in organic materials, the donor-acceptor heterointerface in simple bilayer solar cells must be placed in close proximity to the bottom electrode. This makes great demands on the planarity of the base layer, since a non-uniform topography can cause adverse shorting through overlying layers. We fabricated indium tin oxide (ITO)/titanium oxide (TiO_x)/fullerene (C_{60})/cyanine dye/molybdenum oxide (MoO_3)/silver (Ag) solar cells with TiO_x layers deposited via sputtering, coated from a nanoparticle suspension or prepared via a sol-gel process. A power conversion efficiency of 3.7% was measured when using a smooth sol-gel derived TiO_x film. © *2013 AIP Publishing LLC*. [http://dx.doi.org/10.1063/1.4804599]

Thin, dense films of TiO_x have recently emerged as promising functional layers in hybrid inorganic-organic[1] and purely organic solar cells (OSCs). TiO_x layers have been used as optically transparent spacers to optimize the absorption within the active organic film and were a key component for the fabrication of solution-processed tandem OSCs.[2,3] TiO_x layers were used in the regular (substrate/hole selective contact/active organic layer/TiO_x/metal) and the inverted (substrate/TiO_x/active organic layer/hole selective contact/metal) cell architecture.[4–7] For both device geometries, TiO_x is the electron-selective contact and thus forms the cathode. TiO_x works as an effective barrier that prevents penetration of oxygen and water. In addition, TiO_x acts as an active scavenging layer for removing oxygen and water[8] enhancing the lifetime of OSCs considerably.[5,7]

OSCs with highest power conversion efficiencies (η) use organic films that are applied from a blend of an electron-accepting soluble fullerene derivative with a donor polymer ($\eta = 9.2\%$ (Ref. 9)) or small molecule ($\eta = 7\%$ (Ref. 10)) that form a bulk heterojunction (BHJ). Alternatively, the two organic components can be deposited one by one to create a planar bilayer heterojunction. The efficiency of bilayer OSCs is limited by the small geometrical junction area but is still in use for rapid screening purposes of molecules or when control over the nanoscale phase separation between the components in a blend film is challenging.[11] In addition, a smooth and well-defined planar organic/organic interface is prerequisite to study fundamental opto-electronic processes at organic heterointerfaces.[12]

The active components in an OSC must intimately be in contact on a length scale of well below ~50 nm. This critical distance corresponds to the exciton diffusion length (L_{ex}) of organic semiconductors, and light absorption in regions further away from the heterointerface does not result in free charge carrier generation.[13] The constraint of a small L_{ex} results in an important difference between the required substrate smoothness a BHJ or a bilayer OSC is built on. In bilayer OSCs, the heterointerface is placed at a distance of only $\sim L_{ex}$ away from the bottom electrode, and a non-uniform topography of the substrate can cause shorting through other layers, resulting in low shunt resistance, high dark currents, and poor device performance. The substrate planarity is less critical for BHJ OSCs with typical active film thicknesses of 100–200 nm.

Cyanine dyes (Fig. 1(a)) are actually organic salts that are strongly incompatible with common apolar organic semiconducting materials. This makes the adjustment of a suitable BHJ morphology challenging. However, the very high light extinction coefficients of cyanines compensate for the exciton diffusion bottleneck, and thin (~30 nm) dye films were used in OSCs produced in the regular and inverted bilayer configuration.[14–16]

Here, we investigated different TiO_x films as electron-selective base layers for the fabrication of inverted cyanine OSCs. TiO_x layers were deposited onto glass/indium tin oxide (ITO) substrates (Thin Film Devices, resistivity 20 Ω/sq, 150 nm thickness, root mean square, rms, roughness after cleaning 0.51 nm). For films (samples A-C) deposited via reactive magnetron sputtering (ATC Orion, AJA International), the sputtering gas consisted of argon-oxygen mixtures (O_2 partial pressures between 26% and 89%) at a total pressure of 4×10^{-3} mbar, and a titanium metal disk (99.999%) was used as the target.[17] Alternatively, films (sample D) were spin coated from a TiO_x nanoparticle (Ø ~ 9 nm) suspension (Solaronix, Ti-Nanoxide HT-L/SC).[18] As a further method, crystalline TiO_x films (sample E) were prepared via a sol-gel

---

[a)] E. Berner and T. Jäger contributed equally to this work
[b)] Author to whom correspondence should be addressed. Electronic mail: roland.hany@empa.ch.

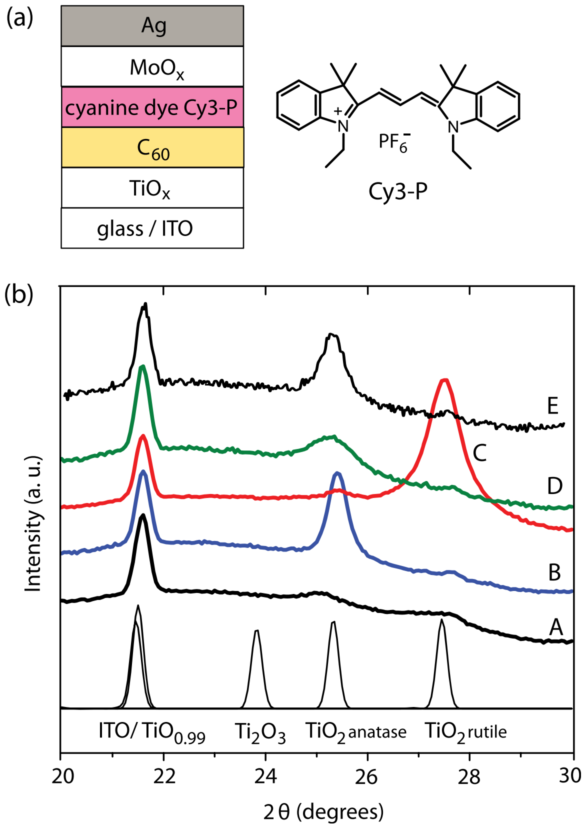

FIG. 1. (a) Schematic representation of the inverted bilayer solar cell. (b) X-ray diffraction patterns of sputtered TiO$_x$ films (samples A and B, thickness ~40 nm, C ~ 110 nm), a nanoparticulate TiO$_x$ film (sample D ~ 45 nm) and a sol-gel derived film (sample E ~ 50 nm) prepared by spin coating on glass/ITO substrates.

process using titanium iso-propoxide as precursor.[19] Amorphous TiO$_x$ films were spin coated onto the substrates using a 0.45 μm filter. Films were then heated within 3 h to 460 °C in air, were kept for 2 h at that temperature, and were then cooled down to room temperature.

Crystallinity of the deposited films was investigated by X-ray diffraction (XRD, Kristalloflex D5000, Bruker). Therefore, the incident angle of the X-ray beam was fixed at an angle of 1° (θ), and the sensor was scanned between 20 and 30 2θ using a step increment of 0.05 2θ. Nearly amorphous films (sample A, Fig. 1(b)) were deposited using rf sputtering (13.4 MHz, 200 W) at a O$_2$ partial pressure of 89% without heating the substrate. Phase-pure anatase films (sample B, Fig. 1(b)) were obtained via rf sputtering by increasing the substrate temperature to 200 °C and using an oxygen content of 57% in the sputtering gas. We note that films deposited on glass via rf sputtering were mostly amorphous, suggesting that ITO functions as a seed layer that promotes crystallization. Phase-pure rutile films on glass or ITO (sample C, Fig. 1(b)) could be produced by dc sputtering (O$_2$ content 26%, substrate 200 °C). Phase-pure anatase was present in the nanoparticle dispersion (sample D, Fig. 1(b)) and produced in the sol-gel derived film after sintering (sample E, Fig. 1(b)).

The film surface topography was characterized with AFM (Mobile S, NanoSurf). Sputtered phase-pure anatase films (Fig. 2(a)) were smooth (rms roughness = 0.7 nm, peak-to-valley height, R$_t$ = 9 nm), and a very similar planar topography was observed for amorphous films (rms roughness = 0.3 nm, R$_t$ = 7 nm). Phase-pure rutile films (Fig. 2(b)) displayed a columnar texture with spikes protruding from the surface (rms roughness = 7.3 nm, R$_t$ = 71 nm). Also, the topography of the nanoparticulate TiO$_x$ film (Fig. 2(c)) was clearly non-planar (rms roughness = 11.5 nm, R$_t$ = 94 nm). However, the steepness of the individual spikes observed for the rutile surface was absent and the surface texture resembled a rolling hills morphology. Very planar surfaces were finally observed for the sol-gel derived films (rms roughness 0.9 nm, R$_t$ = 8 nm, Fig. 2(d)).

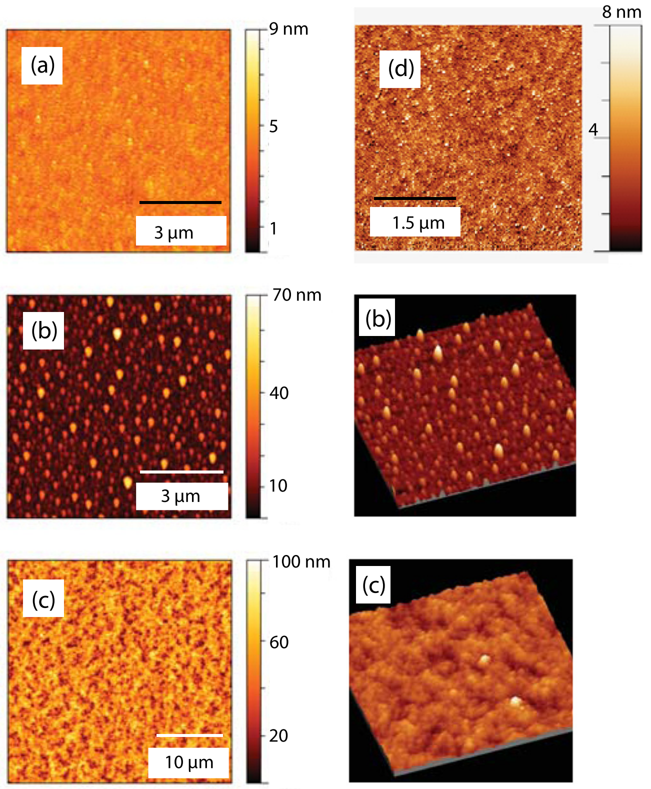

FIG. 2. AFM images of (a) a rf sputtered anatase TiO$_x$ film (sample B), (b) a dc sputtered rutile TiO$_x$ film (sample C), (c) a spin-coated nanoparticulate TiO$_x$ film (sample D), and (d) a sol-gel derived TiO$_x$ film (sample E).

Multilayer OSCs (Fig. 1(a)) were fabricated under N$_2$ atmosphere using glass/ITO/TiO$_x$ substrates A-E. C$_{60}$ (40–80 nm) and MoO$_3$ (5–30 nm) layers with different thicknesses were deposited by thermal evaporation ($<5 \times 10^{-6}$ mbar). Ag (60 nm) was evaporated through a shadow mask to define solar cells with active areas of 3.1 mm^2 or 7.1 mm^2. Cy3-P (FEW Chemicals) films (16–20 nm, $\lambda_{max,film} = 577$ nm (Ref. 14)) were spin coated onto C$_{60}$ from 2,2,3,3-tetrafluoropropanol (TFP) solutions. The UV-vis absorption spectrum of a C$_{60}$ film remained unchanged when repeatedly spin coated with pure solvent, confirming that the fullerene is completely insoluble in TFP.

Current-voltage (J-V) characteristics (Fig. 3) were measured under N$_2$ using 100 mW cm^{-2} simulated AM1.5G solar irradiation on a calibrated solar simulator (Spectra-Nova). The performance characteristics were in accordance with the condition that a smooth and low-resistive TiO$_x$ base layer is required for the fabrication of efficient bilayer heterojunction solar cells. For the spiked rutile substrate (sample C), a high dark current with negligible rectification between forward

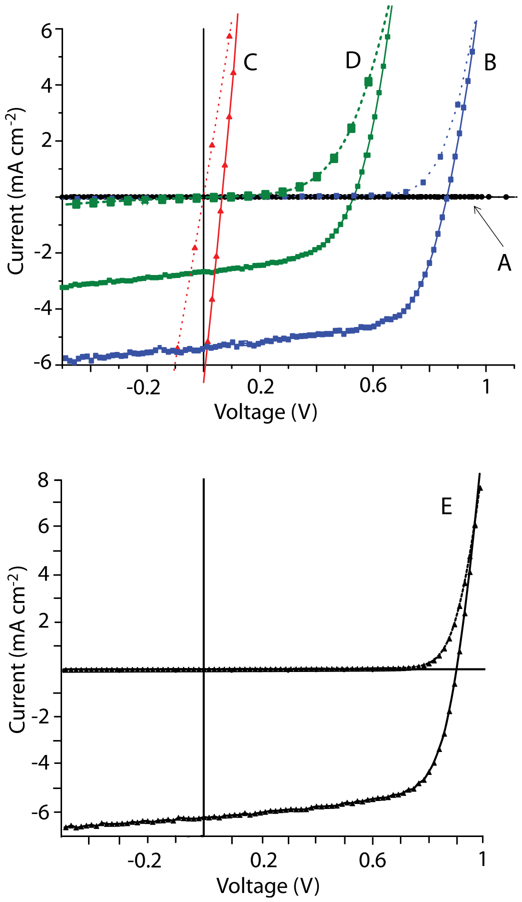

FIG. 3. J-V characteristics of glass/ITO/TiO_x/C_{60}/Cy3-P(16–20 nm)/MoO_3 (30 nm)/Ag(60 nm) OSCs using different TiO_x layers (A = sputtered, amorph; B = sputtered, anatase; C = sputtered, rutile; D = spin coated nanoparticle suspension, anatase; E = sol-gel process, anatase). Dottet lines indicate dark currents, solid lines are currents under light illumination (100 mW cm^{-2}). The C_{60} layer thickness was 40 nm for samples A-C and E, and 80 nm for sample D.

and reverse bias was observed. This is the characteristic for short circuit conditions resulting in a low fill factor (FF) and open circuit voltage (V_{oc}) for the device under illumination. Negligible performance was also observed for the smooth but amorphous TiO_x layer (sample A). In this case, the cathode was completely blocking ($V_{oc} = 0.48$ V, FF = 21.2%, short circuit current, $J_{sc} = 1 \times 10^{-3}$ mA cm^{-2}) consistent with the low conductivity of amorphous TiO_x resulting in a device-limiting series resistance for film thicknesses above ~10 nm.[5]

OSCs performances increased for anatase TiO_x layers B, D, and E with decreasing rms roughnesses and R_t values (Fig. 3). To compensate for the pronounced waviness of the spin coated nanoparticulate TiO_x base layer, the C_{60} layer thickness was increased to 80 nm for sample D. This resulted in decent device performance with a low J_{sc} (2.7 mA cm^{-2}), however (Table I). Incident photon-to-current conversion efficiency (IPCE) curves shown in Refs. 14 and 15 for Cy3-P/C_{60} bilayer solar cells demonstrate that a considerable fraction of current is generated in the wavelength region where C_{60} absorbs light. The reduced current for sample D can, therefore, probably be attributed to ineffective photoexcitation of C_{60} far away from the heterointerface where oxidative charge transfer and current generation occur (L_{ex} C_{60} ~ 40 nm (Ref. 13)).

In addition, also V_{oc} (0.52 V) for sample D was lower than for B ($V_{oc} = 0.84$ V) and E ($V_{oc} = 0.88$ V). In recent work, V_{oc} has been shown to be correlated to the redox energy levels of the active donor and acceptor materials.[4] Specific reasons have been identified that limit V_{oc}, such as reverse saturation current, interfacial charge transfer states, or bimolecular charge recombination.[20] For sample D, we consider that also shunt conduction contributes to the lowering of V_{oc}. The parallel resistance allows for leakage currents from sources such as pinholes. Considering the roughness of the spin-coated nanoparticulate TiO_x layer, pinholes in the active Cy3-P and C_{60} layers can indeed be expected, leading to direct contact of the organic materials with both electrodes at the same time. These direct paths between anode and cathode act as a shunt resistance in parallel with the active part, resulting in a lowered V_{oc} and eroding the device efficiency partly. Parallel resistance values (R_p) in the dark were determined from the inverse of the slope ($\Delta J/\Delta V$) at short-circuit (V = 0). The slope of J(V = 0) was obtained by a least squares fit of a linear curve to the experimental data in the linear regime, [−0.2 V, +0.2 V] in our case. R_p was 2.6 kΩ cm^2 for sample D. For samples B and E, dark current densities were significantly suppressed ($R_p = 9$ kΩ cm^2 for B, 26.5 kΩ cm^2 for E), consistent with reduced leakage current. Note that the spin-coated TiO_x dispersion was used as a base layer in BHJ OSCs using a thickness of 200 nm for the organic film.[18]

Best solar cell performances were measured when using the sol-gel derived TiO_x base layer (sample E, Table I). The highest efficiency was $\eta = 3.7\%$, with an average performance

TABLE I. Device performance/parameters from bilayer C_{60}/Cy3-P solar cells.

Device	V_{oc} (V)	J_{sc} (mA cm^{-2})	FF (%)	η (%)	Ref.
B, sputtered,[a] best	0.84	5.4	63	2.9	This work
B, average 4 cells	0.83 ± 0.1	4.5 ± 0.9	62.2 ± 1.1	2.3 ± 0.5	This work
D, spin coated nanoparticle suspension	0.52	2.7	53.6	0.8	This work
E, sol-gel process, best	0.88	6.2	67.8	3.7	This work
E, average 25 cells	0.86 ± 0.02	6.6 ± 0.8	58.2 ± 4.1	3.3 ± 0.4	This work
ITO/ZnO/PCBM/Cy3-P/MoO_3/Ag[b]	1	1.5	43	0.6	16
ITO/MoO_3/Cy3-P/C_{60}:BCP/Ba:Ag[b]	0.92	5.1	62	2.9	15
ITO/PANI:DBS/Cy3-P/C_{60}/Alq_3/Al[b]	0.72	6.9	61	3.0	14

[a] Different fabrication processes for the phase-pure anatase TiO_x layers were used.

[b] ZnO = zinc oxide, PCBM = [6,6]-phenyl-C_{61}-butyric acid methyl ester, BCP = bathocuproine, Ba = barium, PANI:DBS = polyaniline doped with dodecylbenzenesulfonic acid, Alq_3 = tris-(8-hydroxyquinoline) aluminium.

from 25 cells of $\eta = (3.3 \pm 0.4)\%$. These findings present a considerable improvement compared to reported efficiencies for bilayer fullerene/Cy3-P OSCs in the normal and inverted device geometry so far (Table I).[14–16] We also note that initial measurements of the stability of inverted cyanine solar cells showed promising results. Cells were stable when stored in the glove box for several months, and no sign of degradation was observed under illumination ($50\,\mathrm{mW\,cm^{-2}}$) in nitrogen (for 24 h) or ambient atmosphere (for 6 h).

In conclusion, our results emphasize experimentally the importance of the planarity of the crystalline TiO_x base layer onto which efficient inverted cyanine dye/C_{60} bilayer OSCs could be fabricated. The promising results ($\eta = 3.7\%$) using simple bilayer devices with small interfacial donor-acceptor area demonstrate the potential of cyanine dyes for OSC application. As an important advantage, cyanines are relatively cheap and are commercially available in large quantities. For cyanines with broader absorption spectra or by using mixtures of cyanines that absorb sunlight over the whole visible and into the near-infrared region,[21] it is anticipated that efficiencies can be increased further. In practice, best OSCs were fabricated for TiO_x films produced by a sol-gel process. TiO_x sputtering of thin films for OSCs applications could be an interesting alternative. Sputtering is a large-area compatible coating technology. In addition, the sputter process temperature of 200 °C to deposit phase-pure anatase TiO_x layers would be compatible with polymer-based substrates that are interesting for the development of flexible OSCs. This is in contrast to the sol-gel route that required a high-temperature (>450 °C) annealing step to induce crystallization.

This work was supported by the Swiss Competence Center for Energy and Mobility, CCEM-CH, Dursol project.

[1] M. Helgesen, R. Søndergaard, and F. C. Krebs, J. Mater. Chem. **20**, 36 (2010).
[2] J. Y. Kim, S. H. Kim, H.-H. Lee, K. Lee, W. Ma, X. Gong, and A. J. Heeger, Adv. Mater. **18**, 572 (2006).
[3] J. Y. Kim, K. Lee, N. E. Coates, D. Moses, T.-Q. Nguyen, M. Dante, and A. J. Heeger, Science **317**, 222 (2007).
[4] R. Steim, F. R. Kogler, and C. J. Brabec, J. Mater. Chem. **20**, 2499 (2010).
[5] A. Hayakawa, O. Yoshikawa, T. Fujieda, K. Uehara, and S. Yoshikawa, Appl. Phys. Lett. **90**, 163517 (2007).
[6] C. Waldauf, M. Morana, P. Denk, P. Schilinsky, K. Coakley, S. A. Choulis, and C. J. Brabec, Appl. Phys. Lett. **89**, 233517 (2006).
[7] C.-Y. Li, T.-C. Wen, T.-H. Lee, T.-F. Guo, J.-C.-A. Huang, Y.-C. Lin, and Y.-J. Hsu, J. Mater. Chem. **19**, 1643 (2009).
[8] S. Cho, K. Lee, and A. J. Heeger, Adv. Mater. **21**, 1941 (2009).
[9] Z. He, C. Zhong, S. Su, M. Xu, H. Wu, and Y. Cao, Nature Photon. **6**, 591 (2012).
[10] T. S. van der Poll, J. A. Love, T.-Q. Nguyen, and G. C. Bazan, Adv. Mater. **24**, 3646 (2012).
[11] W. Kylberg, P. Sonar, J. Heier, J.-N. Tisserant, C. Müller, F. Nüesch, Z.-K. Chen, A. Dodabalapur, S. Yoon, and R. Hany, Energy Environ. Sci. **4**, 3617 (2011).
[12] A. Tada, Y. Geng, Q. Wei, K. Hashimoto, and K. Tajima, Nature Mater. **10**, 450 (2011).
[13] P. Peumans, A. Yakimov, and S. R. Forrest, J. Appl. Phys. **93**, 3693 (2003).
[14] B. Fan, F. A. de Castro, B. T.-T. Chu, J. Heier, D. Opris, R. Hany, and F. Nüesch, J. Mater. Chem. **20**, 2952 (2010).
[15] O. Malinkiewicz, T. Grancha, A. Molina-Ontoria, A. Soriano, H. Brine, and H. J. Bolink, Adv. Energy Mater. **3**, 472 (2013).
[16] O. Malinkiewicz, M. Lenes, H. Brine, and H. J. Bolink, RSC Adv. **2**, 3335 (2012).
[17] P. Zeman and S. Takabayashi, Surf. Coat. Technol. **153**, 93 (2002).
[18] D.-S. Leem, A. Edwards, M. Faist, J. Nelson, D. D. C. Bradley, and J. C. de Mello, Adv. Mater. **23**, 4371 (2011).
[19] M. J. Alam and D. C. Cameron, J. Sol-Gel Sci. Technol. **25**, 137 (2002).
[20] A. Maurano, R. Hamilton, C. G. Shuttle, A. M. Ballantyne, J. Nelson, B. O'Regan, W. Zhang, I. McCulloch, H. Azimi, M. Morana, C. J. Brabec, and J. R. Durrant, Adv. Mater. **22**, 4987 (2010).
[21] R. Hany, B. Fan, F. A. de Castro, J. Heier, W. Kylberg, and F. Nüesch, Prog. Photovoltaics **19**, 851 (2011).